Ph.D. DISSERTATION

Structural and electrical characterization of oxide heterointerfaces for 2-dimensional electron gas and water splitting photoanodes

By

Taemin Ludvic Kim

August 2018

DEPARTMENT OF MATERIALS SCIENCE AND ENGINEERING

COLLEGE OF ENGINEERING

SEOUL NATIONAL UNIVERSITY

Structural and electrical characterization of oxide heterointerfaces for 2-dimensional electron gas and water splitting photoanodes

Advisor: Prof. Ho Won Jang

by

Taemin Ludvic Kim

A thesis submitted to the Graduate Faculty of Seoul National University
in partial fulfillment of the requirements
for the Degree of Doctor of Philosophy
Department of Materials Science and Engineering

July 2018

Approved
by

Chairman of Advisory Committee: Seungwu Han

Vice-Advisory Committee: Ho Won Jang

Advisory Committee: Seung-Hyub Baek

Advisory Committee: Sanghan Lee

Advisory Committee: Jin Young Kim

Abstract

Since the heterointerface between different materials possesses various properties that is required in devices, “It may be said that the interface is the device”. In particular, conductivity manipulation at the heterointerface is one of the key technologies to manufacture semiconductor devices, as controlling the movement of electric charges to exhibit desired characteristics is required in electronic devices.

Oxide composites are considered to be promising materials for many devices with various physical phenomena such as high-k dielectrics, high-temperature superconductivity and excellent ferroelectricity. As atomic scale deposition control has become possible with the recent technological development, novel properties which have not been found in bulk materials of natural systems have been discovered. Application studies on these novel properties have been actively carried out.

In this theses, the possibility of controlling the lateral and vertical charge transfer by using the novel phenomena occurring at the heterojunction interface of the oxide composite is proposed. To accomplish this, three

major studies were conducted.

The first is the lateral carrier transport control of the two-dimensional electron gas in oxide heterointerface. The formation of two-dimensional electron gas at the heterointerface between $SrTiO_3$ and $LaAlO_3$ has been reported in 2004. The conductivity of the two-dimensional electron gas can be tuned depending on the degree of tilting of TiO_6 octahedrons in the $SrTiO_3$ substrate. The conductivity can be manipulated by inserting $CaTiO_3$ which has tilted octahedrons. In addition, distortion of the TiO_6 octahedrons are found in the study.

The second is the vertical charge transfer control through band offset management. $LaAlO_3$ is a material with a large dipole moment, which can influence the charge transfer at the heterojunction interface by utilizing the intrinsic electric field induced by the dipole moment. Schottky junctions are formed between Nb-doped $SrTiO_3$ and WO_3, and the Schottky barrier serves as a barrier for electrons to be transferred between materials. However, it has been shown that by inserting $LaAlO_3$ interlayer at the interface, the Schottky barrier can be eliminated and Schottky junction can be effectively replaced with an Ohmic junction.

The third is a charge transfer enhancement study using sequential type II junctions in a photoelectrochemical water splitting device. Heterostructures having a type II junction are often used in the photoanode material constituting photoelectrochemical water splitting cells. A photoelectrode having improved light absorption, photo-conversion efficiency, and electron-hole charge separation capability can be constructed by stacking three materials having a heterojunction structure composed of sequential type II junctions.

In this thesis, lateral and vertical charge transport control in the oxide heterojunction interface through the above studies are shown. This can be applied to electronic devices and solar water splitting cell. This thesis provide a basis for studying the properties of heterogeneous junctions.

Keyword: Electron, Carrier transport, Photoelectrochemical water splitting, Heterojunction, Oxide thin film

Student Number: 2013-23036

Taemin Ludvic Kim

Table of Contents

List of Tables

List of Figures

1. Introduction

1.1. Background and outline of the thesis

Interfacial phenomena are attracting extensive interest with both fundamental and practical points of view since the properties vary with the attached substances and their applicability. The interface between different materials in heterostructures play an important role in many devices such as transistors, lasers, and solar cells.[1,2] Thus, “It may be said that the interface is the device.”, stated Herbert Kroemer in his Nobel lecture.[1]

Nowadays, the heterojunction interfaces of oxide materials are demonstrating various phenomena such as superconductivity, magnetism, ionic conduction, and ferroelectricity.[3, 4] Oxide materials with these phenomena have a wide range of applications including fuel cells, batteries, information storage and more. In particular, oxide interfaces offer the unique opportunity to enhance and control the effects by finely tuning the interaction between layers. Thus, by manipulating the lateral and vertical charge transport at oxide heterointerfaces, desired property

can be achieved for various applications.

In this theses, we expand the understanding of the charge transport in lateral and vertical direction at oxide heterointerfaces. This thesis contains an introduction chapter (Chapter 1) that briefly outlines the thesis and provide scope and objective of the thesis.

Chapter 2 treats the TiO_6 octahedral tilt in perovskite oxide that result in abrupt conductivity change at the $LaAlO_3/CaTiO_3/SrTiO_3$ oxide heterostructure. The formation of 2-dimensional electron gas (2DEG) at the interface between two insulating oxides, $LaAlO_3$ and $SrTiO_3$, is reported in 2004.[5] 2DEG in oxide heterostructure is highly correlated with the TiO_6 octahedral tilt in substrate. Since $CaTiO_3$ has tilted TiO_6 octahedrons, tilted TiO_6 octahedrons will be observed by inserting $CaTiO_3$ at the interface between $LaAlO_3/SrTiO_3$. In this heterostructure, 2DEG conductivity can be tuned not gradually but abruptly depending on the thickness of $CaTiO_3$ layer thickness.

Chapter 3 discuss about band offset tailoring of oxide heterojunction via insertion of atomically thin $LaAlO_3$ perovskite layer for enhanced water splitting properties. Perovskite $LaAlO_3$ which is composed of $(LaO)^+$

plane and $(AlO_2)^-$ plane when deposited in [001] direction, has dipole moment. Band offset can be tailored with this dipole moment to reduce or remove Schottky barrier which can be formed in the interface of a Schottky contacted heterojunction and improve conductivity. By applying this phenomenon in the water splitting photoelectrode system, enhanced interfacial conductivity and superior water oxidation performance is observed.

Enhancing water splitting performance with sequential type-II junctions produced by $Fe_2O_3/BiVO_4/WO_3$ ternary heterostructured oxide layers has been studied in Chapter 4. Many attempts have been made to construct bilayer heterojunction but ternary heterostructure has not been reported yet. In this chapter, enhanced water splitting property with ternary heterostructure is displayed. Ternary heterostructure which consists sequential type-II heterojunction is constructed with Fe_2O_3, $BiVO_4$, and WO_3 for enhanced water oxidation performance.

The summary and conclusions are in Chapter 5.

1.2. Scope and objective of the thesis

This thesis focuses on the manipulation of the lateral and vertical charge transport at the oxide heterointerfaces by using pulsed laser deposition technique. For practical use, tuning the conductivity of the device is essential. High on/off ratio switching and memory devices can be fabricated with oxide materials when the conductivity of the device is completely controlled. In addition, water splitting photoelectrode which can be produced with oxide materials with their photoactivity, high resistance for photocorrosion, and earth abundance also needs fine conductivity and charge transfer resistance control to enrich the water splitting performance.

In this thesis, firstly, lateral charge transfer at the oxide heterointerface between $LaAlO_3$ and $SrTiO_3$, which is names as 2DEG, is tuned by introducing $CaTiO_3$ interlayer which lead to the TiO_6 octahedral tilt. Secondly, vertical charge transfer between photoactive oxide materials have been modified by inserting atomically thin polar insulating $LaAlO_3$ layer between WO_3 and Nb-doped $SrTiO_3$. Finally, photo-generated charge separation in water splitting photoanode is studied by

constructing sequential type-II heterojunction.

Electrons in oxide 2DEG system is confined in ~1 nm, which enables the miniaturization of devices such as field effect transistors. Photoelectrodes with enhanced charge separation efficiency will bring about the commercially available water splitting cells. Lateral conductivity modification studied in this thesis will contribute to commercial use of oxide 2DEG. Furthermore, Schottky barrier removal which is demonstrated by the insertion of $LaAlO_3$ interlayer between WO_3 and Nb-doped $SrTiO_3$ will also provide a deep understanding and insight for fabricating devices. Lastly, enhanced photo-generated charge separation with sequential type-II junctions will lead to the commercialization of water splitting photoelectrode system. The research presented in this thesis further expands the understanding and applicability of oxide heterostructure system.

1.3. References

[1] H. Kroemer, *Rev. Mod. Phys.* **2000**, *73*, 449.

[2] J. Mannhart, D. G. Schlom, *Science.* **2010**, *327*, 1607.

[3] *Nat. Mater.* **2012**, *11*, 91.

[4] A. Brinkman, M. Huijben, M. van Zalk, J. Huijben, U. Zeitler, J. C. Maan, W. G. van der Wiel, G. Rijnders, D. H. A. Blank, H. Hilgenkamp, *Nat. Mater.* **2007**, *6*, 493.

[5] A. Ohtomo, H. Y. Hwang, *Nature* **2006**, *441*, 120.

2. TiO_6 octahedral tilt and distortion in perovskite oxide that result in metal-insulator transition at the $LaAlO_3/CaTiO_3/SrTiO_3$ oxide heterostructure

2.1. Introduction

Recently, oxide heterointerface has captivated researchers since, curiously, electrons in the heterointerface show different property from bulk material such as insulator-to-metal transition at the interface between two insulating perovskite oxides. Electrons which take part in the magnetic and electronic properties of transition metal oxides are frequently originated from d-orbitals. Electrons, which are highly interacting each other in spatially confined d-orbitals, have rich of electronic phases and ordered motion to show insulating (solid), metallic (liquid and gaseous) and superconducting (superfluid) properties as shown in Figure 2.1.[1] These electronic phases are competing each other in a subtle balance and can be affected by external stimuli such as applied electric field, magnetic field, pressure or others, giving rise to a drastic response to these stimuli.[2] In this chapter, metal-insulator transition in

oxide heterointerface will be covered.

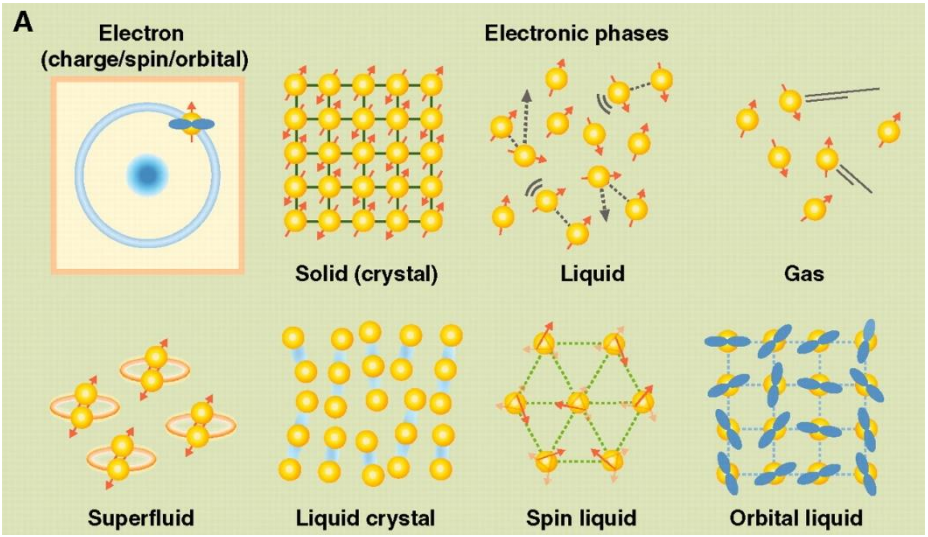

Figure 2.1 A variety of electronic phases formed by correlated electrons.[1]

2.1.1. Perovskite oxide materials

Perovskite is a type of material that has the same structure with calcium titanate ($CaTiO_3$), known as perovskite structure. The structure is firstly found in 1839 and named after Russian mineralogist Lev Perovski. General chemical formula of perovskite oxides is ABO_3, where A is a cation in the body center and B is cations in the corner and O is oxygen ion in the face center as described in Figure 2.2. Thus, perovskite oxides

can be described as a network of BO_6 octahedrons based on the cubic A matrix.

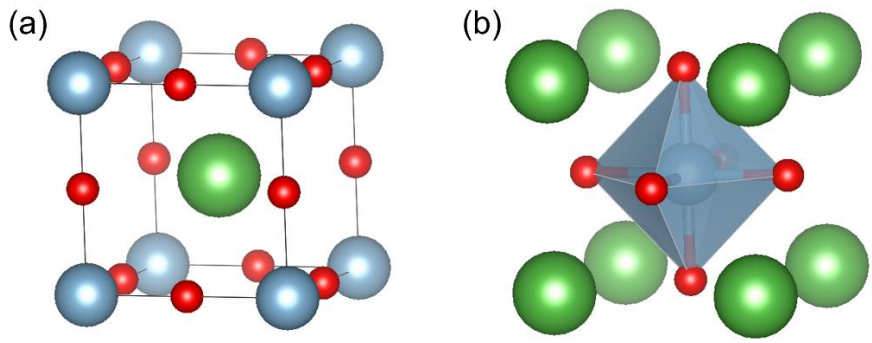

Figure 2.2 (a) Unit cell of ABO_3 perovskite structure with A atom in the body center and B atoms at the corners. (b) Unit cell of ABO_3 perovskite structure with B atom in the body center and A atoms at the corners.

Crystallographic behavior of perovskite oxides is of great interest of researchers since they can possess various structures. The perovskite structure is stable with a large number of metallic elements. Although most of the perovskites are close to an ideal cubic structure, depending on the size of the A and B cations, perovskite oxides would have various crystal structures such as cubic, tetragonal, orthorhombic, rhombohedral, and monoclinic. The stable structure is determined with the tolerance

factor *t* in the following equation:

$$t = \frac{R_A + R_O}{\sqrt{2}(R_B + R_O)}$$

Where R_A, R_B, and R_O are the ionic radii of A and B site elements and oxygen, respectively. The oxide has stable cubic perovskite structure when $t = 1$. When $t > 1$, which means that B cation is relatively smaller than A cation, oxides would have off-centered structure, generating dipoles and ferroelectricity. BO_6 octahedrons would have distorted structure such as $BiFeO_3$ when $t < 1$, which indicates that A cation is relatively smaller than B cation. This tilting affects magnetic and charge transport properties of perovskite oxides since B-O-B angle is reduced, leading to the decrease of orbital overlap and superexchange interaction. The lattice distortion of perovskite oxides is not only governed by the size of the cations but also can be affected by temperature, pressure, chemical composition and electric field.

2.1.2. 2-dimantional electron gas at oxide heterointerface

2DEG is built up of electrons possible to transport in x- and y- directions

whereas firmly confined in z-direction. 2DEG was firstly discovered at the interface between conventional III-V semiconductors. The interesting physics was also found in oxide heterointerfaces between two insulating perovskite insulators, $LaAlO_3$ (LAO) and $SrTiO_3$ (STO). In 2004, Ohtomo and Hwang reported 2-dimensional electron gas (2DEG) in the LAO/STO heterointerface.[3] LAO is deposited on TiO_2 terminated STO (001) single crystal as shown in Figure 2.3. High electron density ($\sim 10^{14}$ cm^{-2}), high carrier mobility ($\sim 10^4$ cm^2/Vs), and low sheet resistance (10^{-2} Ω/sq) are observed in the heterointerface without any dopant (Figure 2.4). LAO/STO heterostructure with $(AlO_2)^-/SrO$ interface is found to be insulating in any conditions.

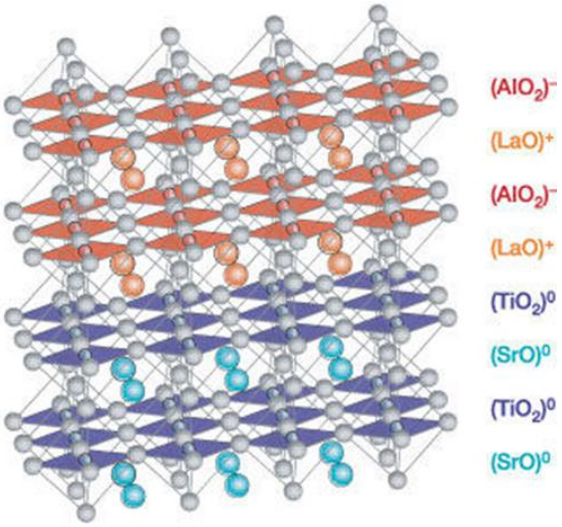

Figure 2.3 Schematic of LAO/STO heterostructure in (001) orientation with (TiO_2)-$(LaO)^-$ interface.[3]

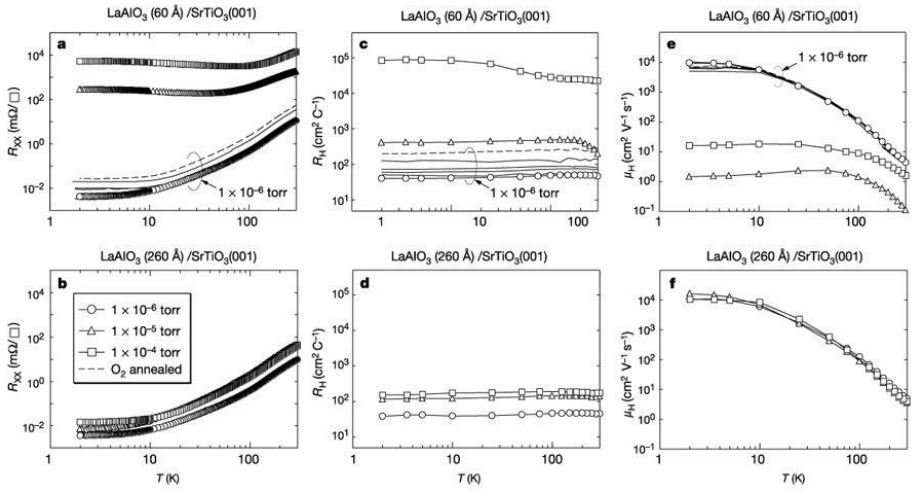

Figure 2.4 Charge transport properties at the interface of LAO/STO heterostructure.[3]

The interface is found to be conducting only when the thickness of LAO film on STO is thicker than critical thickness of 4 unit cells (uc).[4] Insulator-to-metal transition does not occur when the thickness is below the critical thickness, which is an interesting point in this phenomenon.

This 2DEG at the oxide heterointerface is a fascinating electronic system with fascinating properties including magnetism,[5] ferromagnetism,[6] two-dimensional superconductivity below 250 mK,[7] coexistence of superconductivity and ferromagnetism,[8] enhanced Rashba spin-orbital coupling,[9] and strong electric field effect.[10, 11] Conducting width of the 2DEG at oxide heterostructure is narrow up to 2 nm at 300 K whereas the conducting width of 2DEG at III-V semiconductor interface is about 100 nm, which enables the construction of smaller electronic devices. Complex combinations among spin, charge, and orbital degree of freedom make a wide variety of possible electronic phases. Electronic phase change results in the drastic response to external stimuli, by which 2DEG at oxide interface can be applied in sensors, transistors, and memories. Additionally, 2DEG at oxide heterointerface possesses

principle advantages in device scaling with the high electron densities (10^{22} – 10^{23} cm^{-3}) even in the insulating phases. Thus, 2DEG at the oxide interface has a numerous potential with scientific and practical impacts in future oxide electronic devices.

2.1.3. Origin of 2-dimensional electron gas at oxide heterointerface

The mechanism generating 2DEG at the oxide heterointerface is still on debating. To explain the interfacial conductivity, three hypotheses are suggested: polar catastrophe model, cation intermixing model, and oxygen vacancy model as described in Figure 2.5. The scenarios described in each models are not mutually exclusive, hence, multiple mechanism may be relevant.

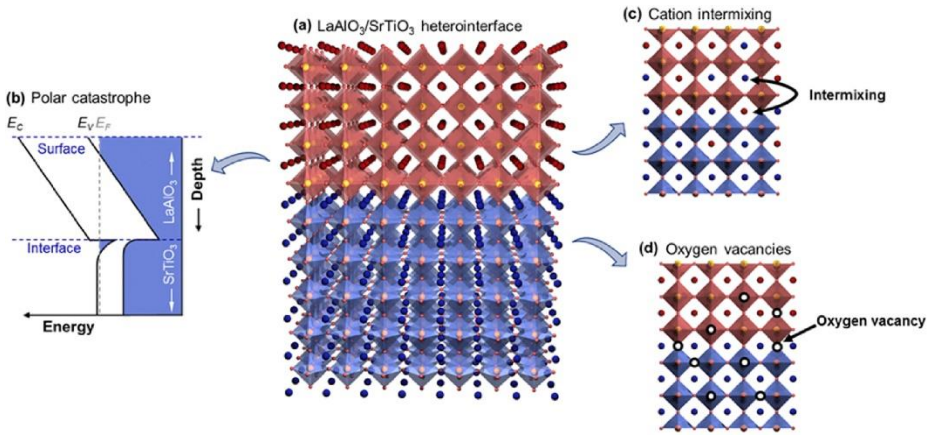

Figure 2.5 The three hypothesis that explains the origin of 2DEG in LAO/STO heterointerface. (a) The atomic structure of LAO/STO heterostructure. La, Al, Sr, Ti, and O atoms are colored with red, yellow, blue, orange, and coral, respectively. (b) Electronic reconstruction due to polar catastrophe. (c) Cation intermixing in the interface. (d) Oxygen vacancies.[12]

Polar catastrophe model

The polar catastrophe model, or electronic reconstruction, was firstly suggested theory to explain metallic electronic properties in oxide heterointerface.[3, 13] The (001) planes in ABO_3 perovskite structure is composed of AO and BO_2 alternating layers. Since oxygen usually has O^{2-} valence, A and B cations can take $A^{4+}B^{2+}$, $A^{3+}B^{3+}$, $A^{2+}B^{4+}$ or $A^{+}B^{5+}$

values to maintain charge neutrality of ABO_3 perovskite oxides. When the cations have $A^{2+}B^{4+}$ valence, non-polar AO and BO_2 layers are alternating in [001] direction such as STO. $(AO)^+$ and $(BO_2)^-$ layers are stacked in sequence when the cations have $A^{3+}B^{3+}$ valence, which is the case of LAO.

Joining perovskite oxides from two different valence charge families in [001] orientation would result in a polar discontinuity at the interface. STO has SrO and TiO_2 neutral layers where LAO has polar $(LAO)^+$-$(AlO_2)^-$ polar layers. `Thus, a sharp transition between polar and non-polar sheets occur at the interface. Electrostatic potential across LAO increases linearly with the thickness of LAO film as depicted in Figure 2.6a. The electrostatic potential diverges to have large values since charged $(LaO)^+$ and $(ALO_2)^-$ planes are sequentially stacked. In this case, some electrons move from LAO to the interface to reduce their Coulombic energy by occupying Ti 3d states, resulting in the valence change of Ti ion from Ti^{4+} to Ti^{3+}, and electrostatic potential accumulation can be removed by the electron migration (Figure 2.6b). Because of the electrons in these Ti 3d states at the 2-dimensional interface, high carrier density, high charge mobility, and low sheet

resistance is observed. In other words, electronic reconstruction is a way to compensate the polar catastrophe at the oxide heterointerface with an abrupt polar/non-polar interface.

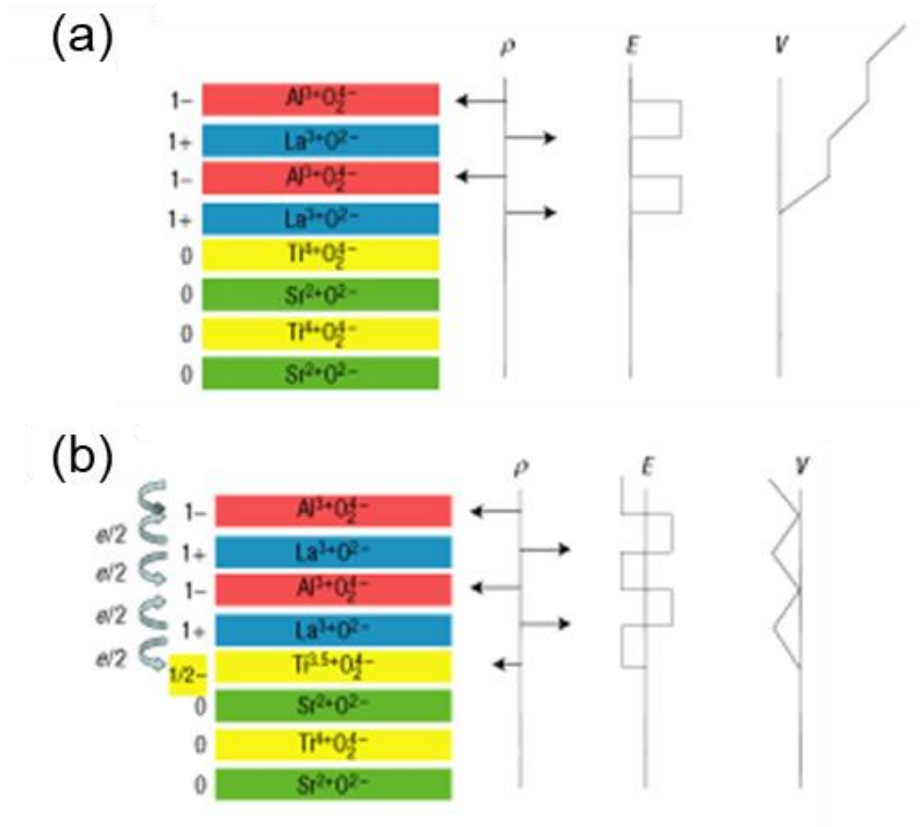

Figure 2.6 The illustration of polar catastrophe model.[13]

Ohtomo and Hwang explained the reason why highly conductive 2DEG at the heterostructure is found only when STO is terminated with TiO_2 surface with this model, since only Ti ion can have multiple valence charge among the ions.[3] In addition, the driving force for electron migration to change Ti valence would be insufficient with the thickness thinner than the critical thickness. However, the polar catastrophe model cannot explain the metallic conductivity at the interface between two nonpolar facets such as amorphous LAO/STO and LAO/STO in [110] orientation.[14, 15]

Cation intermixing model

Another suggested model for the origin of 2DEG at the oxide heterointerfaces is cation intermixing at the LAO/STO interface as depicted in Figure 2.5c. Cation intermixing across the interface can play an important role since the cations have different valence charges. X-ray diffraction and transmission microscopy studies show that the interface cannot be always sharp but has the intermixing between cations.[13, 16] Considering the fact that La-doped STO is conducting compared to the

bare STO since La act as an electron donor, it is reasonable to thick that La an Sr ion mixing at the interface can cause the insulator-to-metal transition at the oxide heterointerface. First principle calculations calculated with classical and quantum mechanical potentials indicated that the cation mixed interface is energetically stable and thermodynamically favorable than the abrupt interface.[17-19]

Nevertheless, cation intermixing model cannot elucidate the insulating interface of LAO/STO heterostructure with $(AlO_2)^-$/SrO interface. In addition, Warusawithana *et al.* argued that stoichiometric ratio of La:Al is a key to have 2DEG at the oxide heterostructure, and metallic conductivity is found only with the excessive Al in the LAO film where the heterostructure with La-rich film is insulating.[20] Thus, cation intermixing itself cannot perfectly clarify the origin of 2DEG at the oxide heterointerface.

Oxygen vacancy model

Oxygen vacancies in oxide films would act as electron donors since one absence of oxygen creates two electrons in the film. Thus, forming

oxygen vacancies during the growth of LAO film would lead to the formation of 2DEG in LAO/STO heterostructure. In the heterointerface between amorphous LAO and STO, oxygen vacancy model is the only possible hypothesis for conducting interface. Since La has a higher oxygen affinity than Sr or Ti in STO, oxygen vacancies are created and valence charge of Ti ions are reduced as LAO is deposited on the STO surface. The measured conductivities of the heterostructure with amorphous and crystalline LAO overlayers are equivalent, indicating that crystallinity is independent for 2DEG conductivity.[21] Thus, oxygen vacancy model is more reasonable rather than polar catastrophe model since crystalline LAO film is required for alternating polar sheets in polar catastrophe model. The fact that oxygen pressure during growth and high temperature annealing affect the conductivity of 2DEG at oxide heterointerface also supports oxygen vacancy model.[14, 21, 22] The metallic properties of the oxide heterostructure with LAO overlayer are diminished abruptly after annealing at oxygen abundant condition. The conductivity at the interface between Al_2O_3 and STO which do not have polar sheets also proves that oxygen vacancies are the carrier source.

2.1.4. Motivation and objectives

After the discovery of 2DEG at oxide heterointerface, many attempts have been made to utilize this phenomenon in devices.[23-25] Recent studies focus on the factors that affecting the metallic 2DEG conductivity such as TiO_6 octahedral tilt, ferroelectric polarization, and external stimuli.[26-29] Moon *et al.* manipulated the 2DEG conductivity by gradually changing the substrate material from STO to $CaTiO_3$ (CTO).[29] SCTO ($Sr_xCa_{1-x}TiO_3$, x = 0, 0.5, 0.75, 0.88 and 1.0) interlayer is inserted between LAO and STO as a pseudo-substrate material to induce TiO_6 octahedral tilt. Since CTO has distorted TiO_6 octahedrons as shown in Figure 2.7, the TiO_6 octahedrons in LAO/SCTO/STO heterostructure would be tilted as Ca composition increases and carriers at the interface localized, resulting in the decrease of the interfacial conductivity. In spite of the research, the relation between octahedral tilt and metallic property of the oxide heterostructure is not studied quantitatively yet.

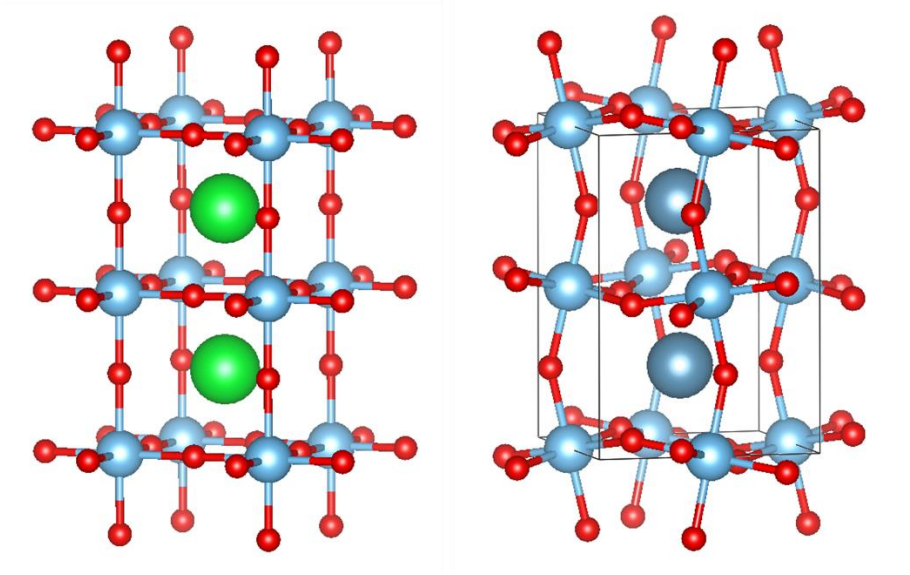

Figure 2.7 Cubic perovskite oxide as STO (left) and orthorhombic perovskite oxide as CTO (right)

Atomic-scale study with transmission electron microscopy (TEM) is indeed needed to investigate and analyze the quantitative TiO_6 octahedral tilting angle. The invention of annular bright field (ABF) imaging in aberration-corrected scanning electron microscopy (Cs corrected STEM) enables to determine the exact position of light elements. As a result, TiO_6 octahedral tilt can be visualized with Cs corrected STEM using the elaborate technique. The objective of this chapter is to unveil the relation

between the degree of octahedral tilt and conductivity of the oxide heterointerface. LAO/CTO/STO heterostructure is constructed with different CTO interlayer thickness to have diverse octahedral tilting angle. The thickness of CTO interlayer is 1-100 uc and the thickness of LAO overlayer is confined as 5 nm. 2DEG at the interface is controlled by tuning the symmetry with various thickness of CTO interlayer. This will provide a pathway to design and utilize oxide heterostructures with 2DEG for multiple functionalities.

2.2. Experimental method

2.2.1. Target preparation

CTO target was synthesized by a conventional solid-state solution method. $CaCO_3$ and TiO_2 powders were dissolved in high-purity ethanol without further purification. The mixture was ball milled homogeneously for 24 hr and dried at 80 ℃ for 24 hr followed by the calcination at 750 ℃ for 4 hr to have $CaTiO_3$. After calcination, CTO is grinded with pestle and mortar and ball milled again for 24 hr with high purity ethanol. Then the mixture is dried for 24 hr. Dried power is sieved and pressed into a round pallet without any binder followed by sintering process at 1300 ℃ for 4 hr. Heating rate was 2 ℃/min for calcination and sintering processes. The whole heating processes were conducted in a box furnace under air ambient condition. After heating, the target was cooled down to room temperature without additional cooling processes.

2.2.2. Epitaxial film growth by pulsed laser deposition method

Prepared CTO pallet and single crystalline LAO is used as targets. KrF

(248 nm) excimer laser is used for pulsed laser deposition method. Epitaxial CTO and LAO is grown on (001) single crystalline STO substrate. STO substrate is firstly cleaned in conventional method with sonicator. After cleaning process, STO substrates were etched in commercially used buffered oxide etchant ($HF:NH_4F = 1:6$) for 30 s to remove surface SrO layer and terminate the surface with TiO_2 layer. Then substrates were annealed in 900 ℃ while expose to blowing air. CTO and LAO were deposited surface treated STO (001) single crystals. STO substrates are attached to the sample holder of the chamber with silver paste. The size of STO samples are typically 5 × 5 mm^2. The oxygen partial pressure during deposition was maintained to be 1 mTorr for both CTO and LAO deposition. Laser power, frequency and heater temperature were 2 J/cm^2, 2 Hz, and 600 ℃, respectively.

2.2.3. TEM analysis

Cross-sectional specimens of LAO/CTO/STO heterostructures were prepared for TEM and STEM using focused ion beam (FIB) milling. Bright field (BF) and High-resolution TEM images were observed with

JEOL JEM-2100F TEM to confirm the quality of the TEM samples. Microstructures of the samples were investigated with JEOL ARM 200F STEM with a probe Cs corrector, using atomically resolved high angle annular dark field imaging (HAADF, collecting angle: 115-276 mrad), and annular bright field imaging (ABF, collecting angle: 11-23 mrad). Oxygen atoms in real space can be depicted with mentioned equipment, thus, projection of the oxygen octahedral network can be imaged. The acceleration voltage was 200 kV. The scanning step for atomic resolution images was 0.06 Å with a dwell time of 16 μs/pixel. The corresponding interfacial chemical distributions were studied with electron energy loss spectroscopy (EELS) with convergence semi angle 19.0 mrad and colleting semi angle 39.6 mrad.

2.3. Result and discussion

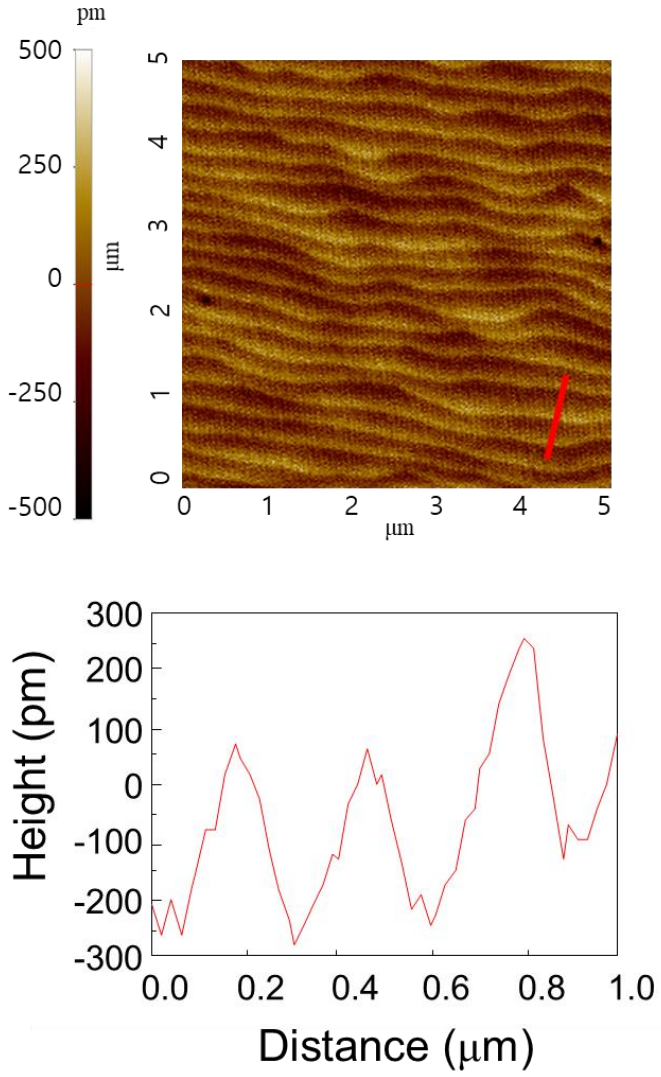

Figure 2.8 Surface AFM image of LAO/CTO (20 uc)/STO heterostructure (upper). The height profile of the red line in upper figure (lower).

LAO/CTO/STO heterostructures were constructed with pulsed laser deposition method. CTO and LAO were deposited in sequence on the surface treated STO which has TiO_2-terminated surface. Atomic force microscopy (AFM) image as shown in Figure 2.8 reveals that particle free surface with the terrace width of 200 nm is obtained after deposition. Terrace height of about 0.4 nm is equivalent with the height of single unit cell of the surface LAO.

Current-voltage curves of LAO/CTO/STO heterostructures with different CTO thicknesses are displayed in Figure 2.9. When the thickness of the CTO interlayer is less than 5 uc, the interface of the heterostructures are conducting, whereas when the thickness of the CTO is thicker than 7 uc, conductivity drops abruptly and shows metal-insulator transition. With the CTO interlayer thickness thicker than 10 uc, conductivities of the samples saturated and become insulating compared to the LAO/STO or LAO/CTO/STO with thin CTO interlayer. Current can be tunes over 5 orders of magnitude as CTO interlayer thickness increases Thus, electrical conductivity of the oxide heterostructure can be tuned with the thickness of CTO interlayer which results in the TiO_6 octahedral tilt in the heterostructure.

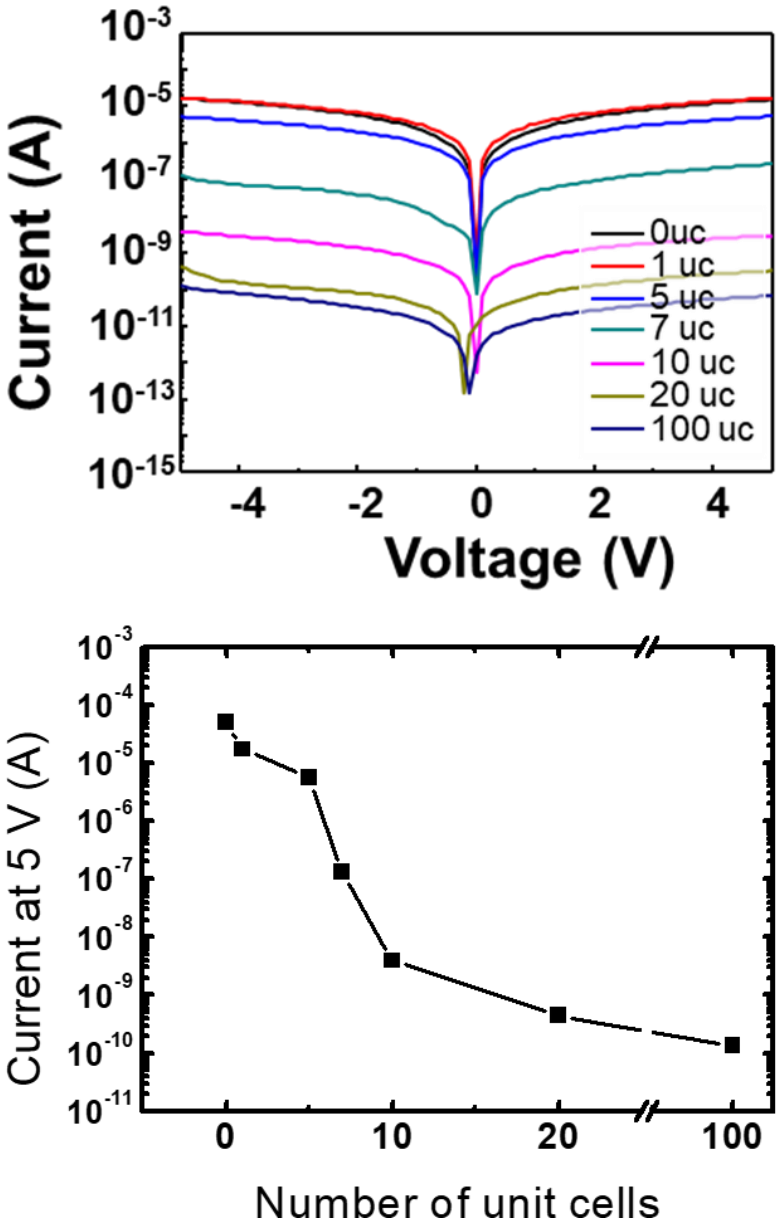

Figure 2.9 (upper) I-V curves of various LAO/CTO/STO with different CTO interlayer thicknesses and (lower) current at 5 V versus number of unit cells of CTO interlayer.

To confirm the origin of conductivity loss at the LAO/CTO interface, HAADF image and EELS is observed as shown in Figure 2.10. Line 6 in Figure 2.10b, Ti $L_{2,3}$ EELS spectra obtained at the heterointerface of LAO/CTO, evidences the presence of Ti^{3+} since the peak near 462 eV are broadened at the interface while distinct sharp four peaks are observed in line 1, far from the LAO/CTO interface. Figure 2.10c also reveals that the amount Ti^{3+} component cannot be ignored as the ratio of Ti^{3+} is *c.a.* 30%, which means the large amount of charges are immobile. In other words, the conductivity loss and metal-insulator transition is not due to the carrier reduction but because of the carrier localizations.

When the BO_6 octahedrons are tilted in ABO_3 perovskite oxides, carriers are localized and become insulating even the material is heavily doped.[26, 30] Thus, interfacial conductivity of LAO/CTO which is depending on the thickness of CTO interlayer reveals that the degree of octahedral tilt relies on the CTO interlayer thicknesses.

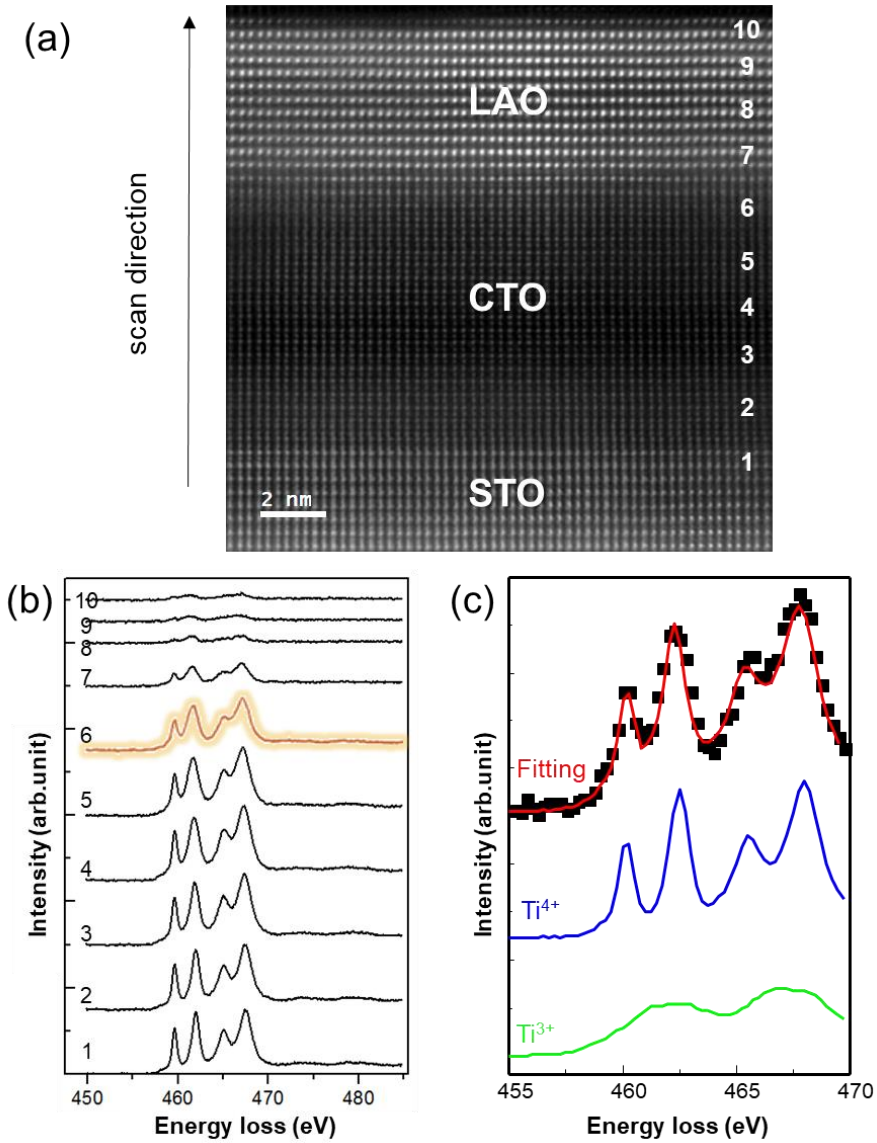

Figure 2.10 (a) HAADF STEM image of LAO/20 uc CTO/STO heterostructure in [110] zone axis. (b) EELS Ti L edge spectra of LAO/CTO/STO heterostructure acquired in 1 nm intervals as marked in (a). (c) Ti^{3+} quantification of line 6 in (b)

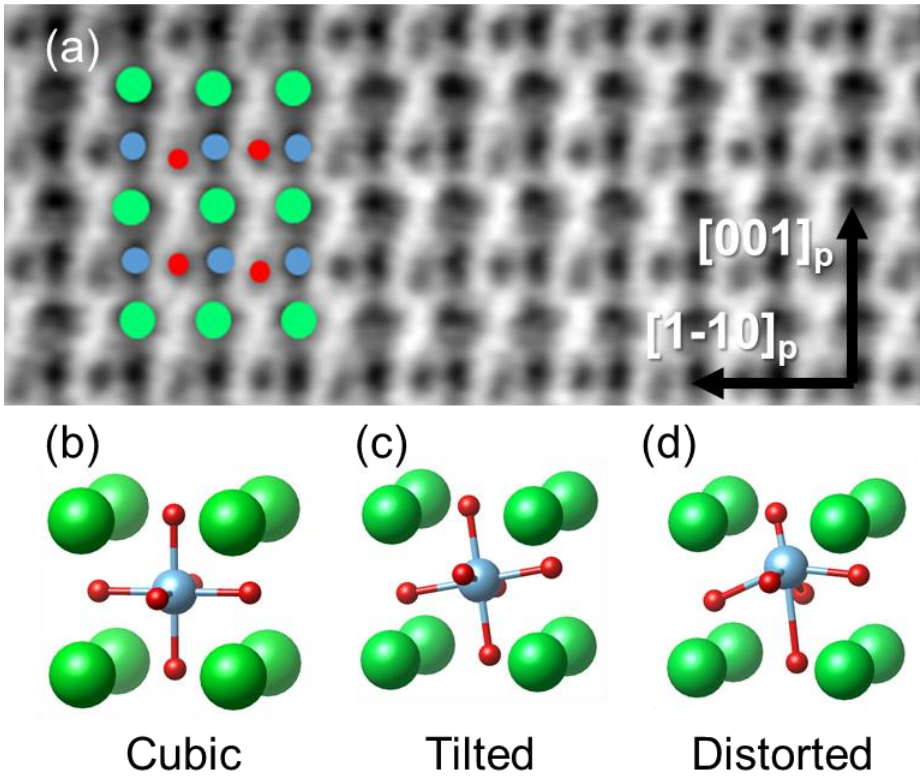

Figure 2.11 (a) ABF STEM image of CTO film in $[110]_p$ zone axis. Green, light blue, and red circles indicate Ca, Ti, and O ions. (b-d) Atomic structure of the stoichiometric CTO with cubic (b), tilted TiO_6 octahedron (c), and distorted TiO_6 octahedron (d) structure.

To confirm the relationship between interfacial conductivity and structural symmetry, ABF STEM image of the LAO/CTO/STO

heterostructure with 20 uc CTO interlayer is observed. Figure 2.11a is the magnified image of CTO interlayer, reveals that TiO_6 octahedrons have distortion. Atomic structure of STO substrate is cubic structure as depicted in Figure 2.11b, and CTO on STO substrate is predicted to have TiO_6 octahedral tilt as shown in Figure 2.11c. Tilted octahedrons would have straight O-Ti-O bonding with the angle of 180° and Ti-O-Ti bonding angle with 153.5°. Oxygen atomic columns shown in Figure 2.11a, however, indicate that the TiO_6 octahedrons are distorted and O-Ti-O angle is smaller than 180° and Ti-O-Ti bonding angle is smaller than 153.5°. The whole ABF STEM image of LAO/CTO/STO is displayed in Figure 2.12a. The image implies that CTO and LAO films are fully strained by the STO substrate and coherently grown on the substrate without a single dislocation. Since ABF STEM image detects the light elements, the exact position of oxygen atomic columns can be specified in the heterostructure. Thus, O-Ti-O and Ti-O-Ti angles vs atomic row marked in Figure 2.12a are plotted in Figure 2.12b and c. Ti-O-Ti represents the tilting angle of TiO_6 octahedrons and O-Ti-O angle designates the degree of the octahedral distortion. Both angles at STO substrate are 180°, whereas both angles decrease and saturate to be 145°

as the atomic position goes far from the CTO/STO heterointerface. This result suggests that the interface coupling is dominant in the CTO film when CTO interlayer thickness is less than 5 uc. Consequently, octahedral tilt and distortion is suppressed and conductivity is not affected. On the other hand, with the thick CTO interlayers thicker than 10 uc, octahedrons are both tilted and distorted with epitaxial strain, inducing metal-insulator transition at LAO/CTO heterointerface.

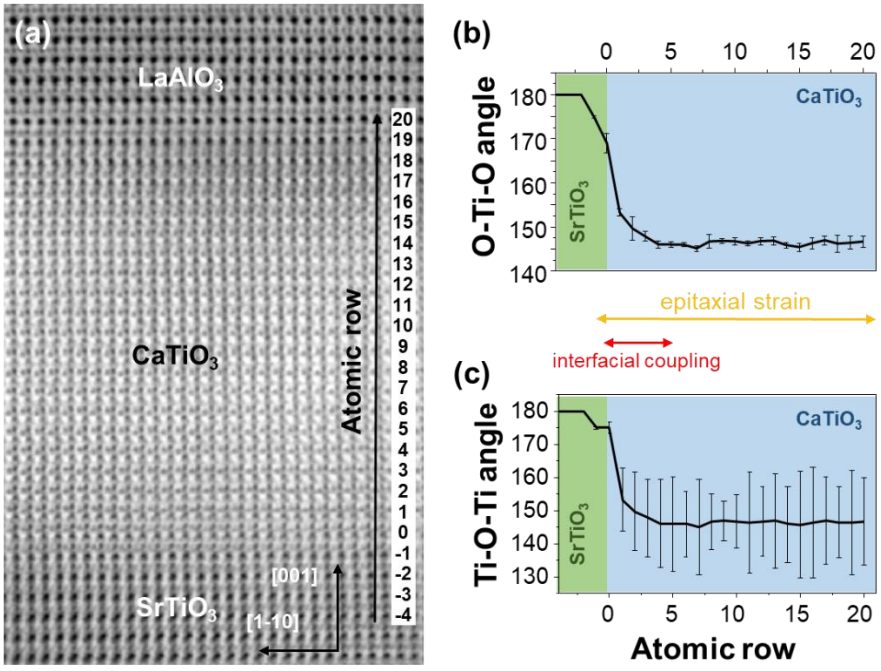

Figure 2.12 (a) ABF STEM image of the LAO/CTO/STO in zone axis of [110]. (b) O-Ti-O bonding angle and (c) Ti-O-Ti bonding angle versus atomic position marked in (a)

In summary, metal-insulator transition is observed with CTO interlayer insertion. When the inserted CTO thickness is more than 5 uc, epitaxial strain induces TiO_6 octahedral tilt and distortion, leading to the conductivity drop of the heterointerface, whereas, when the thickness is less than 5 uc, due to the interfacial coupling, conductivity remains as if the interlayer does not exist. Conductivity drop with TiO_6 octahedral tilt and distortion is not due to the reduction of carrier concentration but because of the localization of carriers as confirmed with EELS. Large amount of Ti^{3+} which can donate electrons exist. However, carriers are immobile with localization when TiO_6 octahedrons are tilted and distorted. Observed tilting angle is about 145° which is smaller than the predicted 153.5°. O-Ti-O angle which indicates the degree of TiO_6 distortion is also about 145°, smaller than the ideal value, 180°. Therefore, with the manipulation of TiO_6 octahedral tilt and distortion which can be induced with epitaxial strain, 2DEG conductivity control is available, which can be applied in fabricating small electronic devices with oxide heterostructures.

2.4. References

[1] H. Takagi, H. Y. Hwang, *Science* **2010**, *327*, 1601.

[2] E. Dagotto, *Science* **2005**, *309*, 257.

[3] A. Ohtomo, H. Y. Hwang, *Nature* **2006**, *441*, 120.

[4] S. Thiel, G. Hammerl, A. Schmehl, C. W. Schneider, J. Mannhart, *Science* **2006**, *313*, 1942.

[5] A. Brinkman, M. Huijben, M. van Zalk, J. Huijben, U. Zeitler, J. C. Maan, W. G. van der Wiel, G. Rijnders, D. H. A. Blank, H. Hilgenkamp, *Nat. Mater.* **2007**, *6*, 493.

[6] B. Kalisky, J. a. Bert, B. B. Klopfer, C. Bell, H. K. Sato, M. Hosoda, Y. Hikita, H. Y. Hwang, K. a. Moler, *Nat. Commun.* **2012**, *3*, 922.

[7] N. Reyren, S. Thiel, A. D. Caviglia, L. F. Kourkoutis, G. Hammerl, C. Richter, C. W. Schneider, T. Kopp, A.-S. Ruetschi, D. Jaccard, M. Gabay, D. A. Muller, J.-M. Triscone, J. Mannhart, *Science* **2007**, *317*, 1196.

[8] J. A. Bert, B. Kalisky, C. Bell, M. Kim, Y. Hikita, H. Y. Hwang, K. a. Moler, *Nat. Phys.* **2011**, *7*, 767.

[9] A. D. Caviglia, M. Gabay, S. Gariglio, N. Reyren, C. Cancellieri, J. M. Triscone, *Phys. Rev. Lett.* **2010**, *104*, 1.

[10] A. D. Caviglia, S. Gariglio, N. Reyren, D. Jaccard, T. Schneider, M. Gabay, S. Thiel, G. Hammerl, J. Mannhart, J.-M. Triscone, *Nature* **2008**, *456*, 624.

[11] Y. Xie, C. Bell, T. Yajima, Y. Hikita, H. Y. Hwang, *Nano Lett.* **2010**, *10*, 2588.

[12] T. L. Kim, H. W. Jang, *Curr. Appl. Phys.* **2017**, *17*, 626.

[13] N. Nakagawa, H. Y. Hwang, D. A. Muller, *Nat. Mater.* **2006**, *5*, 204.

[14] S. Y. Moon, C. W. Moon, H. J. Chang, T. L. Kim, C.-Y. Kang, H.-J. Choi, J.-S. Kim, S. H. Baek, H. W. Jang, *Electron. Mater. Lett.* **2016**, *12*, 243.

[15] A. Annadi, Q. Zhang, X. Renshaw Wang, N. Tuzla, K. Gopinadhan, W. M. Lü, A. Roy Barman, Z. Q. Liu, A. Srivastava, S. Saha, Y. L. Zhao, S. W. Zeng, S. Dhar, E. Olsson, B. Gu, S. Yunoki, S. Maekawa, H. Hilgenkamp, T. Venkatesan, Ariando, *Nat. Commun.* **2013**, *4*, 1838.

[16] P. R. Willmott, S. A. Pauli, R. Herger, C. M. Schlepütz, D. Martoccia, B. D. Patterson, B. Delley, R. Clarke, D. Kumah, C. Cionca, Y. Yacoby, *Phys. Rev. Lett.* **2007**, *99*, 155502.

[17] L. Qiao, T. C. Droubay, V. Shutthanandan, Z. Zhu, P. V Sushko, S. A. Chambers, *J. Phys. Condens. Matter* **2010**, *22*, 312201.

[18] L. Qiao, T. C. Droubay, T. C. Kaspar, P. V. Sushko, S. A. Chambers, *Surf. Sci.* **2011**, *605*, 1381.

[19] S. A. Chambers, M. H. Engelhard, V. Shutthanandan, Z. Zhu, T. C. Droubay, L. Qiao, P. V. Sushko, T. Feng, H. D. Lee, T. Gustafsson, E. Garfunkel, A. B. Shah, J. M. Zuo, Q. M. Ramasse, *Surf. Sci. Rep.* **2010**, *65*, 317.

[20] M. P. Warusawithana, C. Richter, J. a Mundy, P. Roy, J. Ludwig, S. Paetel, T. Heeg, A. A. Pawlicki, L. F. Kourkoutis, M. Zheng, M. Lee, B. Mulcahy, W. Zander, Y. Zhu, J. Schubert, J. N. Eckstein, D. A. Muller, C. S. Hellberg, J. Mannhart, D. G. Schlom, *Nat. Commun.* **2013**, *4*, 2351.

[21] W. Siemons, G. Koster, H. Yamamoto, W. A. Harrison, G. Lucovsky, T. H. Geballe, D. H. A. Blank, M. R. Beasley, *Phys.*

Rev. Lett. **2007**, *98*, 3.

[22] A. Kalabukhov, R. Gunnarsson, J. Börjesson, E. Olsson, T. Claeson, D. Winkler, *Phys. Rev. B* **2007**, *75*, 2.

[23] S.-I. Kim, D.-H. Kim, Y. Kim, S. Y. Moon, M.-G. Kang, J. K. Choi, H. W. Jang, S. K. Kim, J.-W. Choi, S.-J. Yoon, H. J. Chang, C.-Y. Kang, S. Lee, S.-H. Hong, J.-S. Kim, S. H. Baek, *Adv. Mater.* **2013**, *25*, 4612.

[24] S. I. Kim, H. Jin Gwon, D. H. Kim, S. Keun Kim, J. W. Choi, S. J. Yoon, H. Jung Chang, C. Y. Kang, B. Kwon, C. W. Bark, S. H. Hong, J. S. Kim, S. H. Baek, *Sci. Rep.* **2015**, *5*, 1.

[25] A. Mawrie, T. Kanti Ghosh, *J. Phys. Condens. Matter* **2016**, *28*, 425302.

[26] H. W. Jang, D. a. Felker, C. W. Bark, Y. Wang, M. K. Niranjan, C. T. Nelson, Y. Zhang, D. Su, C. M. Folkman, S. H. Baek, S. Lee, K. Janicka, Y. Zhu, X. Q. Pan, D. D. Fong, E. Y. Tsymbal, M. S. Rzchowski, C. B. Eom, *Science* **2011**, *331*, 886.

[27] C. W. Bark, D. a. Felker, Y. Wang, Y. Zhang, H. W. Jang, C. M. Folkman, J. W. Park, S. H. Baek, H. Zhou, D. D. Fong, X. Q. Pan, E. Y. Tsymbal, M. S. Rzchowski, C. B. Eom, *Proc. Natl. Acad. Sci.* **2011**, *108*, 4720.

[28] V. T. Tra, J. W. Chen, P. C. Huang, B. C. Huang, Y. Cao, C. H. Yeh, H. J. Liu, E. A. Eliseev, A. N. Morozovska, J. Y. Lin, Y. C. Chen, M. W. Chu, P. W. Chiu, Y. P. Chiu, L. Q. Chen, C. L. Wu, Y. H. Chu, *Adv. Mater.* **2013**, *25*, 3357.

[29] S. Y. Moon, D. H. Kim, H. Jung Chang, J. Kwon Choi, C.-Y. Kang, H. Jin Choi, S.-H. Hong, S. H. Baek, J.-S. Kim, H. W. Jang, *Appl. Phys. Lett.* **2013**, *102*, 12903.

[30] M. Imada, A. Fujimori, Y. Tokura, *Rev. Mod. Phys.* **1998**, *70*,

1039.

3. Band offset tailoring of oxide heterojunction via insertion of atomically thin $LaAlO_3$ perovskite layer for enhanced water splitting properties

3.1. Introduction

The recent energy crisis and global warming are all originated from massive use of fossil fuels. The burning of fossil fuels that have been buried for millions of years is one of the main cause of global average temperature rise. Harvesting energy directly from sunlight provides a desirable approach to solving the global energy challenge in these days with minimal environmental impact.[1] However, solar energy has daily and seasonal variation, energy harvested from sunlight is required to be efficiently converted into storable energy sources. Solar energy conversion as an alternative of fossil fuel combustion is therefore receiving a great attention recently.[2-6] Therefore, the aim of the solar energy conversion is to capture the freely available energy from sunlight and convert it into valuable and strategically important asset such as hydrogen.[7]

3.1.1. Water splitting photoelectrochemical cells

Solar water splitting cell is one of the most promising way to separate water into hydrogen and oxygen. Photoelectrochemical water splitting is a carbon free reaction to produce hydrogen and oxygen. Since Fujishima and Honda discovered photolysis of water with n-type TiO_2 in 1972,[8] researchers have been studied photoelectrochemical cells in the past decades.[9-17] Photoelectrochemical cells are composed of anode and cathode which involves water oxidation and reduction reaction, respectively. Among the two reaction, anodic reaction is limiting with slow kinetics involving multi-electron and multi-proton transfer and highly required overpotential. Thus, developing an effective and practical anode system is in high demand for commercially viable photoelectrochemical cells.

The photoanodic half-cell is illustrated in Figure 3.1.[7] When a semiconductor is contacted with an electrolyte, at the beginning, electric current flows from the semiconductor to electrolyte until electronic equilibrium is reached. The transfer of electric charge results in the production of space-charge layer at the surface of semiconductor where

the charge distribution of the material is different from the bulk. Thus, the energy band of the semiconductor is bent to have flat Fermi level equivalent to the redox potential of the electrolyte. The band is bent upward when the position of the Fermi level of the semiconductor is lower than the flat band potential, which is essentially needed for anodic reaction of n-type semiconductor.

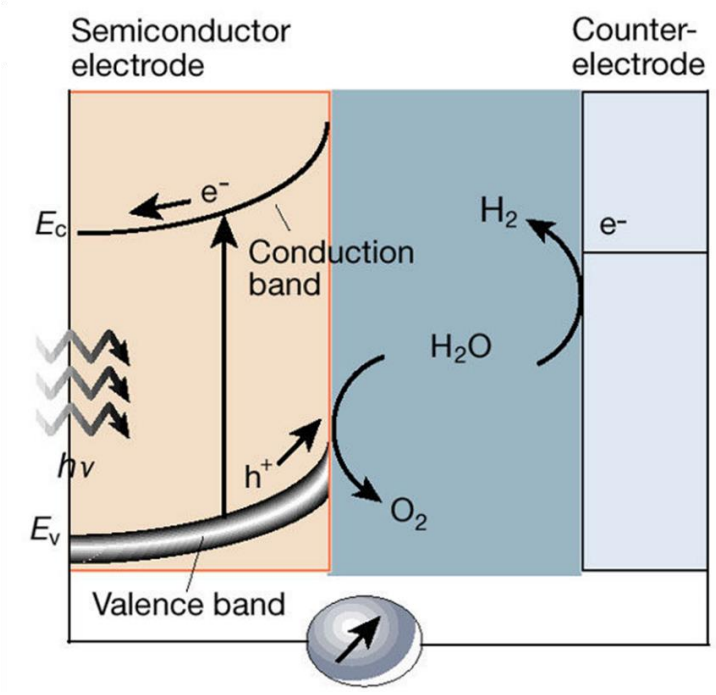

Figure 3.1 Illustration of photoelectrochemical water oxidation half-cell and the corresponding energy band diagram.[7]

Water oxidation in photoanode engages multiple steps such as light absorption, charge separation and transportation, and charge injection to water.[18-21] Light is absorbed to semiconducting photoanode and electrons in the valence band is excited to the conduction band when the absorbed light has higher energy then the band gap of the material. Generated electron-hole pairs are separated with the band bending of the photoanode. Holes are moved to the electrode/electrolyte interface to oxidize water into oxygen and electrons are migrated to counter electrode to produce hydrogen. The overall reaction is the separation of water into hydrogen and oxygen by sunlight. As a consequence, desirable photoanode materials should have an appropriate band gap to absorb sufficient sunlight and to generate electron-hole pairs, long carrier life time for charges to be transported, and thermodynamically favorable valence band edge position that offers overpotential for charge injection to water.[1] Thus, many attempts have been made to find a proper material for photoanodic reaction.

3.1.2. $LaAlO_3$ perovskite oxide

LAO is a wide-gap insulating perovskite oxide with the band gap of 5.6 eV. As mentioned previously in the Chapter 2.1.1, when LAO is deposited in [001] direction, alternating $(LaO)^+$ and $(AlO_2)^-$ is composing LAO perovskite material as shown in Figure 3.2. Alternating polar sheets in [001] direction creates dipole moment of 80.1 meV/Å across LAO in [001] direction.[22] Although LAO has wide band gap that cannot absorb visible light and cannot used as a photoanode, it is used to modulate band offset of other photoactive materials with the internal electric field induced by the dipole moment in this chapter.

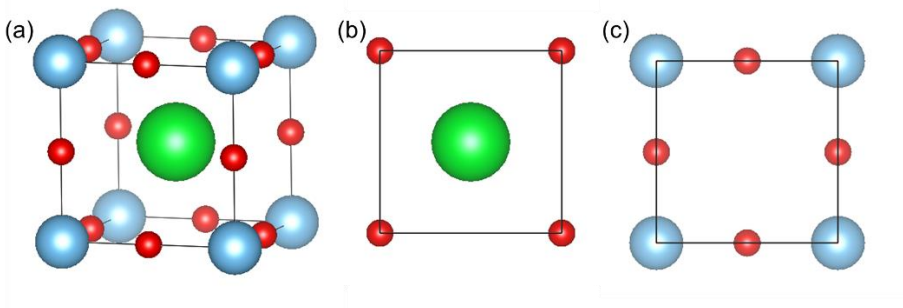

Figure 3.2 (a) Perovskite structure of LAO. (b) $(LaO)^+$ plane in (001) orientation. (c) $(AlO_2)^-$ plane in (001) orientation

3.1.3. Motivations and objectives

The advancement of deposition technique enables the atomic size control of deposition process, leading to the discovery of various captivating phenomena such as electron tunneling,[23, 24] high-temperature superconductivity,[25] and strongly correlated electron systems.[26, 27] Among these phenomena, electron confined system at the oxide heterointerface between two insulating oxides, LAO and STO attracted intensive interest, due to the interesting properties such as magnetism,[28] ferromagnetism,[29] superconductivity below 250 mK,[27] coexistence of ferromagnetism and superconductivity,[30] strong electric field,[31] and switchable electromechanical response.[32] In addition to these attractive behaviors of electrons that are not shown in bulk materials, band offset manipulation and Schottky barrier removing with internal electric field induced by the dipole moment across LAO in [001] direction have been studied recently.[33] Counterintuitively, Schottky contact can become Ohmic contact with the insertion of insulating LAO thin layer. The electrical conductivity is tuned over 7 order of magnitude in the $SrRuO_3$/Nb:STO (001) interface by inserting LAO interlayer between $SrRuO_3$ and Nb:STO. This phenomenon that is theoretically proposed

for innovative photovoltaic devices,[34] can also be applied for water splitting photoelectrode.

WO_3 is one of the promising material for water splitting photoanode with its properly small band gap of 2.7 eV, long carrier diffusion length, and high carrier concentrations. However, the performance of a photoanode does not depend solely on the photoactive material but relying on the contact resistance and charge transfer efficiency between materials that consisting the photoelectrode. Since STO has a lattice constant of 3.905 Å which correspond to the WO_3 lattice, Nb:STO is often considered as a conducting substrate for WO_3. Nevertheless, Schottky barrier which is given by the difference between the Fermi level of the two oxides regulates the charge transfer between oxides and prevents to exploit full potential of WO_3 photoanode for water oxidation. In this chapter, WO_3/LAO/Nb:STO heterostructure is constructed to fully unlock the full potential of WO_3 on Nb:STO substrate. Substantially enhanced water oxidation performance is observed with the LAO interlayer. Internal electric field induced by polar $(LaO)^+$ and $(AlO_2)^-$ sheets reduces Schottky barrier and drive the Schottky contact between WO_3 and Nb:STO Ohmic. Two different charge transfer dynamics are witnessed

in the heterostructure containing LAO interlayer: direct tunneling and Fowler-Nordheim tunneling. This system is also applied for $BiVO_4$ and Fe_2O_3 photoanodes on Nb:STO, which also leading to the removal of interfacial charge blocking barrier. This stimulating phenomenon can be applied for other Schottky contacted oxide materials to remove Schottky barrier.

3.2. Experimental method

3.2.1. Target preparation

WO_3 and Fe_2O_3 powders are molded with pure WO_3 and Fe_2O_3 powders, respectively. Sintering temperature for the WO_3 and Fe_2O_3 targets are 900 ℃ and 1200 ℃, respectively. $BiVO_4$ (BVO) target is made with conventional solid solution process with Bi_2O_3 and V_2O_5 powders are dissolved in ethanol for 24 hr ball milling. 5% excessive Bi is added for stoichiometric $BiVO_4$ film deposition. After ball milling, solution is dried for 80 ℃ for 24 hr. Dried powder is calcined in 760 ℃ for 4 hr for calcination. Calcined powder is grinded into smaller particles followed by sieving and molding into a round pallet. After molding, pallet is sintered in 900 ℃ for 5 hr. heating rate of calcination and sintering is 2 ℃/min. Single crystalline LAO (001) substrate is used as the LAO target.

3.2.2. Film growth by pulsed laser deposition method

KrF (248 nm) excimer laser source is used. Laser power, repetition, and

target to substrate distance is maintained to be 2 J/cm^2, 2 Hz, and 5 cm, respectively, for all film growth. Nb:STO is used as substrate. Substrate temperature during deposition is maintained for 600 ℃ for LAO, WO_3 and Fe_2O_3 deposition and 350 ℃ for BVO deposition. Oxygen pressure for LAO, WO_3, Fe_2O_3 deposition was 100 mTorr and for oxygen pressure for BVO deposition was 200 mTorr. Thickness of all photoactive film (WO_3, BVO, and Fe_2O_3) was measured to be 50 nm with X-ray reflectometry.

3.2.3. Film characterization

The thickness of LAO interlayer is determined by observing atomic scale high-resolution TEM image and STEM image with Cs-corrected TEM. Acceleration voltage for TEM observation was 200 kV. X-ray diffractometer is used to have X-ray diffraction of oxides/LAO/Nb:STO heterostructures. AFM image is witnessed to scan the surface of LAO/Nb:STO.

3.2.4. Photoelectrochemical measurements

Photoactive oxides/LAO/Nb:STO is sealed with resin after made a contact with Cu wire by using In-Ga eutectic alloy and silver paste to prevent current leakage. Photoelectrochemical properties were measured using a three-electrode cell with electrolyte which is made up of 0.5 M Na_2SO_3 and 0.5 M Na_2SO_3 buffer all of which serve as a hole scavenger. Saturated Ag/AgCl electrode is used as a reference electrode and Pt plate is used as a counter electrode. A xenon lamp with AM 1.5 G irradiation filter is used for photocurrent measurement. Voltage step and scan rate were set to be 10 mV and 10 mV/sec, respectively, while linear sweep voltammetry measurement. Considering Nernstian shift, applied voltage during photoelectrochemical measurement is calculated versus reversible hydrogen electrode (RHE) with the following equation.

$$V_{RHE} = V_{Ag/AgCl} + V^0_{Ag/AgCl} + 0.059 \times pH$$

Where $V^0_{Ag/AgCl}$ is 0.197 V and pH of the solution is about 7.

3.3. Result and discussion

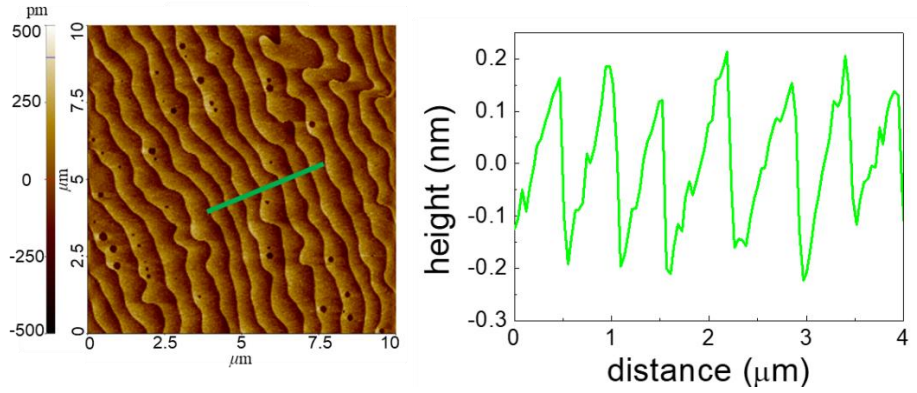

Figure 3.3 (left) AFM image of 3 uc LAO/STO and (right) hieight profile of green line in the left figure.

SrO and TiO_2 layers are alternating in Nb:STO (001) substrate in [001] direction. Since SrO layer is volatile and TiO_2 layer is stable, when the substrate is etched with buffered oxide etchant ($HF:NH_4F$ = 1:6) for 30 sec, surface SrO layer will be eliminated and the surface will be terminated with TiO_2 layer. The surface-etched substrate is then annealed at 900 ℃ in a tube furnace while expose to blowing air. 3 uc of LAO thin film was deposited on the TiO_2-terminated Nb:STO (001) surface. As shown in Figure 3.3, particle free surface, which reveals a high-quality

deposition, is observed with AFM. Terrace width of 500 nm indicates that the miscut of the substrate is about 0.05° and terrace height of *c.a.* 0.4 nm is the same as the height of perovskite LAO single unit cell.

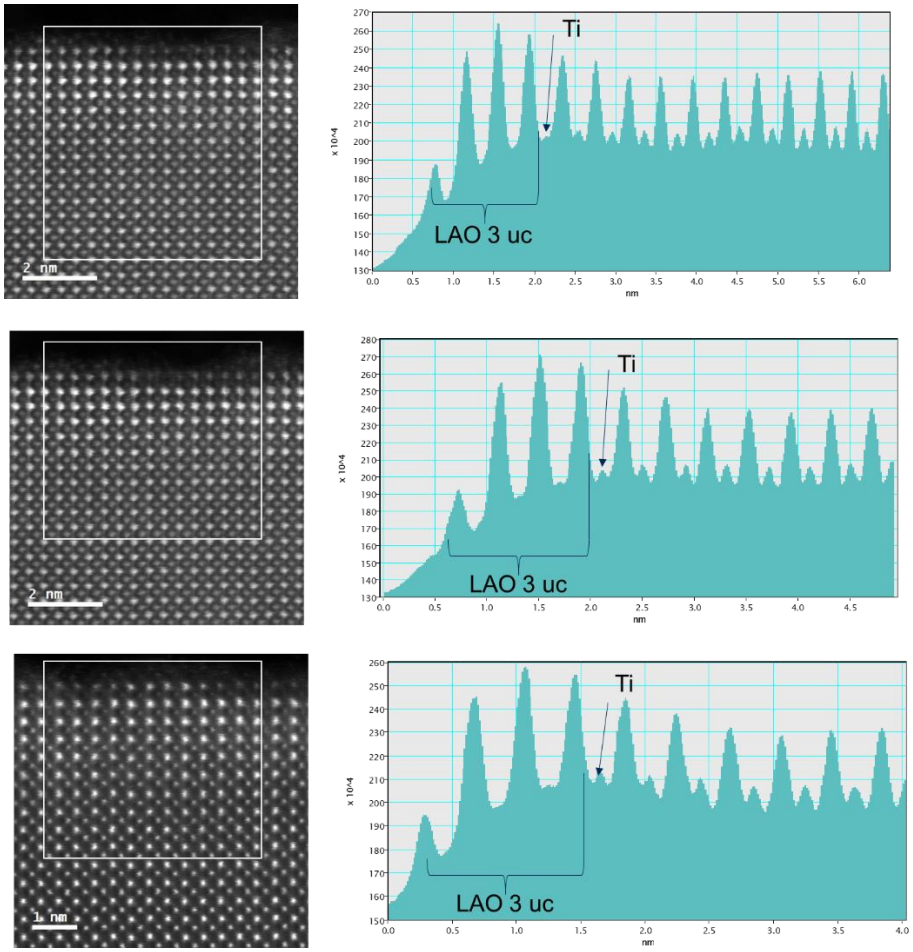

Figure 3.4 HAADF high-resolution STEM images (left figures) and intensity profile (right figures) of 3 uc LAO/Nb:STO heterostructure.

High-resolution HAADF STEM cross sectional image shown in Figure 3.4 reveals that 3 uc of LAO is deposited on TiO_2-terminated Nb:STO substrate. Signal intensity of STEM image is proportional to the atomic weight, therefore, La, Sr, and Ti atoms are shown as the peak in intensity profile while Al and O atoms are now shown in the profile since the atoms are too light to be detected. Four peaks from the surface represents La atoms in LAO and the small peak presenting right after the fourth peak is Ti. Small Ti peak and large Sr peak is alternating as SrO and TiO_2 sheets are composing STO substrate and Sr is heavier than Ti. Since TiO_2 sheet is the termination layer, Ti small peak is at the interface between STO and LAO. Additionally, energy-dispersive X-ray spectroscopy (EDS) of LAO/Nb:STO heterostructure shown in Figure 3.5 also guarantees that thickness of LAO is 3 uc. The signal intensity of La and Sr crosses after four peaks of La from the surface, which indicates that four LaO layer is deposited on the Nb:STO. Four LaO and three AlO_2 sheets consists 3 uc of LAO overlayer on Nb:STO.

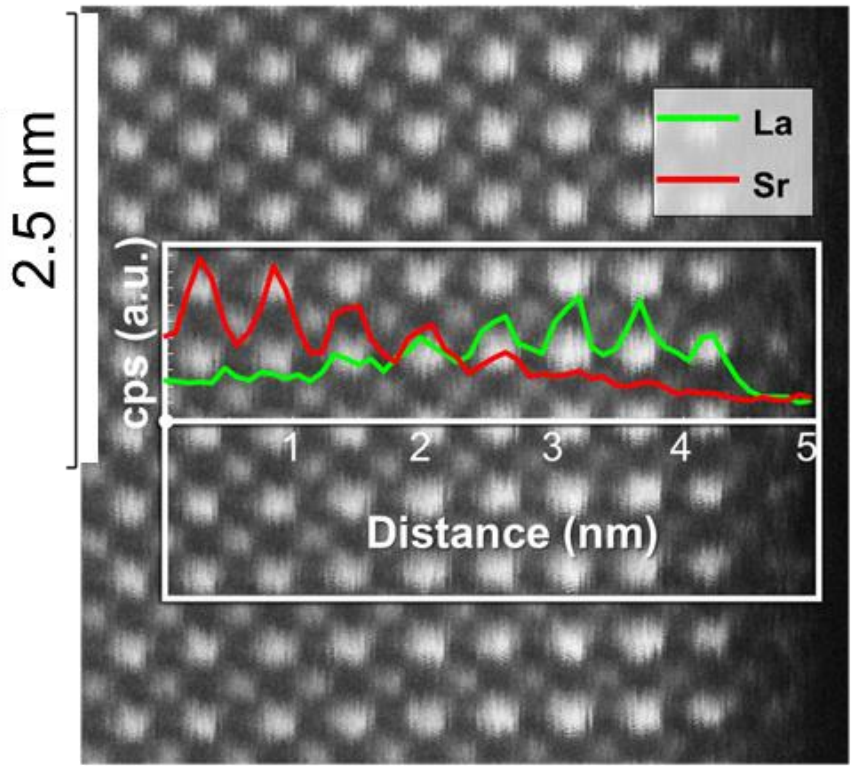

Figure 3.5 EDS line profile of La and Sr atoms in 3 uc LAO/STO heterostructure.

Al and La layers are appeared to be three and four, respectively, on the substrate a shown in EDS mapping data of Al Kα1 and La Lα1 in Figure 3.6 This also points out that 3 uc of LAO layer is deposited on Nb:STO substrate. Thus, deposition condition is calibrated with the results.

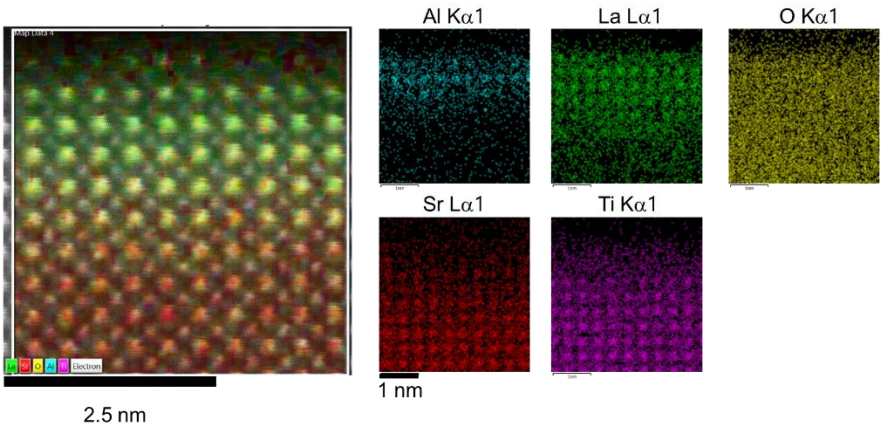

Figure 3.6 EDS mapping of 3 uc LAO/Nb:STO heterostructure.

50 nm WO_3 is deposited on the surface of the LAO/Nb:STO heterostructure. Bright field Figure 3.7a shows the morphology of WO_3 and heterointerface of WO_3/3 uc LAO/Nb:STO in the inset figure. X-ray diffraction scan imply that polycrystalline WO_3 is grown on LAO/Nb:STO heterostructure. LAO interlayer is undetectable with X-ray since the thickness of the interlayer is too thin.

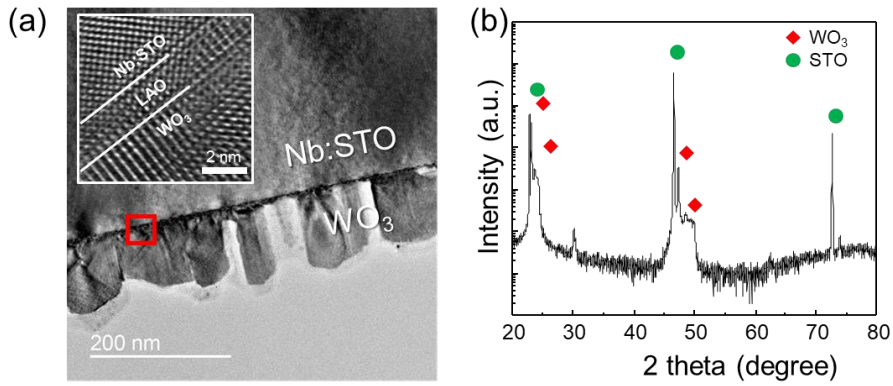

Figure 3.7 (a) TEM image of WO_3/3 uc LAO/Nb:STO and (inset) high-resolution TEM image of red boxed area. (b) X-ray diffraction of WO_3/LAO/Nb:STO.

To measure the effect of LAO interlayer with different thicknesses, LAO and WO_3 is deposited on Nb:STO. LAO thicknesses are ranging from 0 uc (without LAO interlayer) to 6 uc and the thickness of WO_3 is fixed as 50 nm. Photoelectrochemical properties of WO_3/LAO/Nb:STO heterostructure is measured as shown in Figure 3.8. Heterostructures with LAO interlayer present enhanced water oxidizing performance than the sample without LAO interlayer. Photocurrent density of the heterostructures with LAO interlayer converges when the external bias is less than 1 V vs RHE while the current diverges to have different

values when the applied voltage is higher than 1.2 V. Thus, it is reasonable to presume that water oxidation has two distinguishable dynamics with external bias less than 1 V and higher than 1.2 V. Photocurrent density increases as the thickness of LAO interlayer increases until the thickness reaches 3 uc LAO, and decreases when the thickness of the interlayer is thicker than 3 uc (3.5 uc, 4.5 uc and 6 uc). To verify the dynamics of water oxidation and photoreactivity, transient light absorption spectra is measured at 1.23 V vs RHE as shown in Figure 3.8b. Before light illumination, current level of all samples are in the range of ~100 nA/cm^2, while the current density with light illumination was in the range of ~250 μA/cm^2. When WO_3 absorbs light, photo-generated holes will move to the oxide/electrolyte interface and accumulated because of the slow kinetics of water oxidation, or consumed in trap sites such as oxygen vacancies.[35-40] Because of this reason, anodic peak is observed right after light illumination and get relaxed to a steady state. Transient curve of the heterostructure with 3 uc LAO has the highest photocurrent density indicating that the optimal thickness of LAO interlayer in WO_3/LAO/Nb:STO heterostructure is 3 uc.

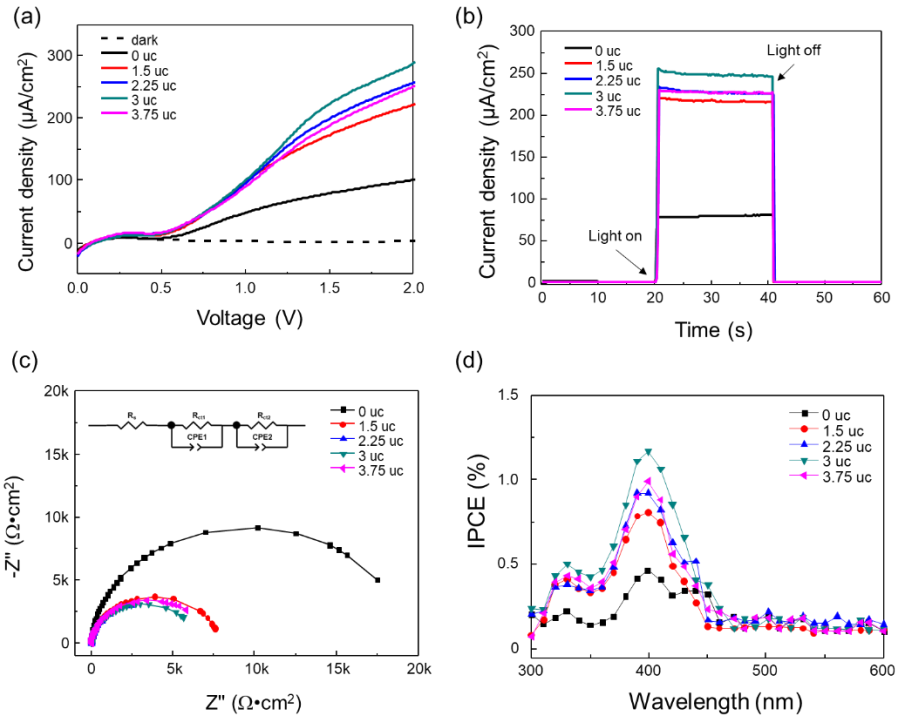

Figure 3.8 Photoelectrochemical properties of WO_3/LAO/STO heterostructure with different LAO interlayer thicknesses. (a) Linear sweep voltammetry curves. (b) Transient absorption spectroscopy. (c) Electrochemical impedance spectra. (d) Incident photon-to-current convertion efficiency curves.

To understand the charge transfer and water oxidation kinetics at the interfaces, electrochemical impedance spectroscopy (EIS) was measured as shown in Figure 3.8c while applying 1.23 V vs RHE and illuminating

light. Frequency range is from 100 kHz to 0.1 Hz. The equivalent Randle circuit is displayed as a inset of Figure 3.8c. The circuit is composed of series resistance, R_s, two charge transfer resistances, R_{ct1} and R_{ct2}, and two constant phase elements, CPE1 and CPE2, representing imperfect capacitors. The smallest semicircle of WO_3/3 uc LAO/Nb:STO indicates that the sample has the smallest charge transfer resistance. The fitted values of R_s, R_{ct1}, and R_{ct2} is presented in Table 3.1. WO_3/3 uc LAO/Nb:STO ha the smallest R_s, R_{ct1}, and R_{ct2} value as 2.882 Ω•cm^2, 7.883 Ω•cm^2, and 6455 Ω•cm^2, respectively, indicating that the heterostructure with 3 uc LAO interlayer has the smallest charge transfer resistance between oxides. This reflects that the Schottky barrier which blocks the charge transfer between WO_3 and Nb:STO is reduced or removed with insertion of LAO interlayer. In addition, charge transfer at WO_3/electrolyte interface is also improved with the 3 uc LAO interlayer, which contribute to the band offset modification of the heterostructure with internal electric field induced by polarization.

Table 3.1 Series resistance (R_s) and charge transfer resistances (R_{ct}) across interfaces of WO_3/LAO/Nb:STO heterostructure.

Number of LAO interlayer	R_s [Ω cm^2]	R_{ct1} [Ω cm^2]	R_{ct2} [Ω cm^2]
0 uc	3.268	19.82	21500
1.5 uc	3.560	13.448	7837
2.25 uc	3.452	9.750	6720
3 uc	2.882	7.883	6455
3.75 uc	4.713	9.274	7118

Incident photon-to-current conversion efficiency (IPCE) in Figure 3.8d also reveals that the heterostructure with 3 uc LAO has the best conversion efficiency. All of the spectra converge to zero at 450 nm which correspond to 2.7 eV, the band gap of WO_3 photoanode.

The enhanced water oxidation performance of heterostructures with LAO interlayer is due to the large internal electric field produced by polar $(LaO)^+$ and $(AlO_2)^-$ sheets. As described in Chapter 3.1.2, LAO deposited in [001] direction has 80.1 meV/Å dipole moment.[22] With 3 uc of LAO, band offset can be manipulated to have V_d as 0.93 eV energy step between WO_3 and Nb:STO as shown in Figure 3.9. Without LAO, contact between WO_3 and Nb:STO is Schottky contact. Therefore,

Schottky barrier blocks photogenerated electrons to pass through the interface. On the other hand, with LAO interlayer, Schottky barrier is removed and photogenerated electrons which possess higher energy with internal electric field can easily transverse LAO interlayer to Nb:STO substrate by tunneling as sub unit cells of LAO layer is negligibly thin. Thus, the heterostructures with atomically thin LAO interlayer present superior photoelectrochemical reaction than toe control sample without LAO interlayer. However, this hypothesis cannot fully explain the reason why photocurrent converges with small external bias and diverges with large bias. To elucidate this phenomena, it is reasonable to assume that there are two different charge transfer dynamics vary with the external bias amplitude: direct tunneling and Fowler-Nordheim (FN) tunneling. Direct tunneling is electron transport through insulating layer directly as shown in Figure 3.9b and FN tunneling is the electron tunneling through triangular barrier as shown in Figure 3.9c. With small external bias, direct tunneling is foremost charge transfer mechanism since the thickness of LAO interlayer is thin enough to travel through, while with larger voltage than 1.2 V, FN tunneling become the main charge transfer dynamics as the Fermi level of WO_3 reach to the triangular barrier.[41-43]

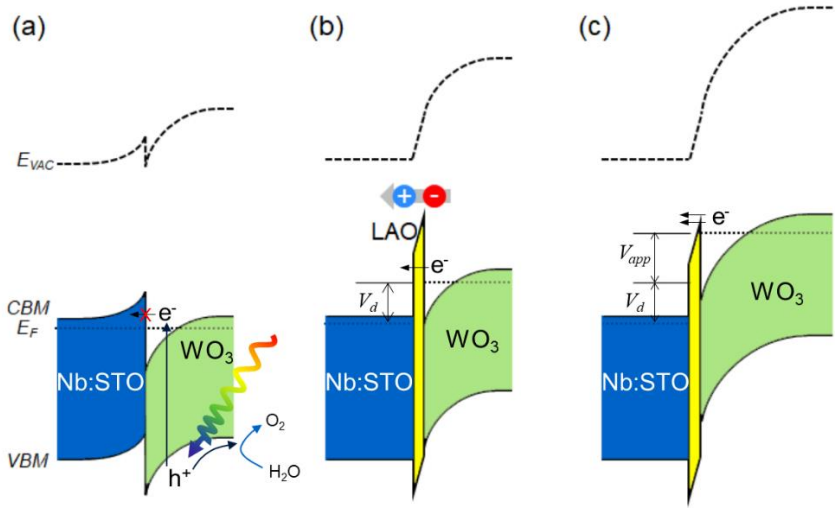

Figure 3.9 Schematic of interface energy band diagrams with or without LAO interlayer.

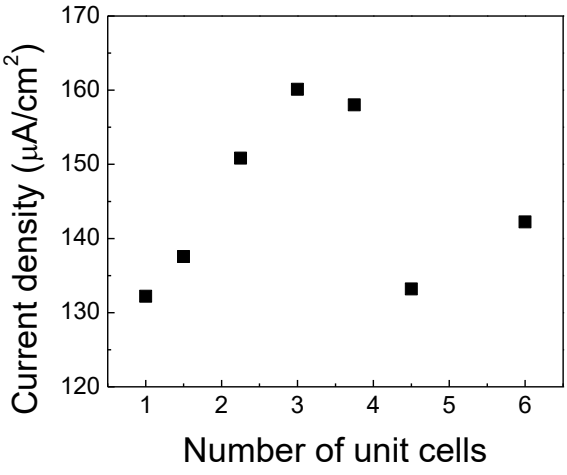

Figure 3.10 Photocurrent density as a function of number of unit cells of LAO at 1.23 V vs RHE.

When the thickness of LAO interlayer getting thicker than 3 uc, energy band of STO substrate adjacent to LAO will be bent downward to have 2DEG at the interface, which is reported in numerous research.[26, 44-47] The bending depth of the STO substrate is about 0.4 eV,[48] results in the reduction of V_d to be 0.53 eV. Thus, water splitting property of WO_3/LAO/Nb:STO heterostructure with 4.5 uc is inferior than the heterostructure with 3 uc LAO interlayer as shown in Figure 3.10. The heterostructure with 6 uc LAO has enhanced water splitting property, which attribute to the heightened V_d with thicker LAO interlayer.

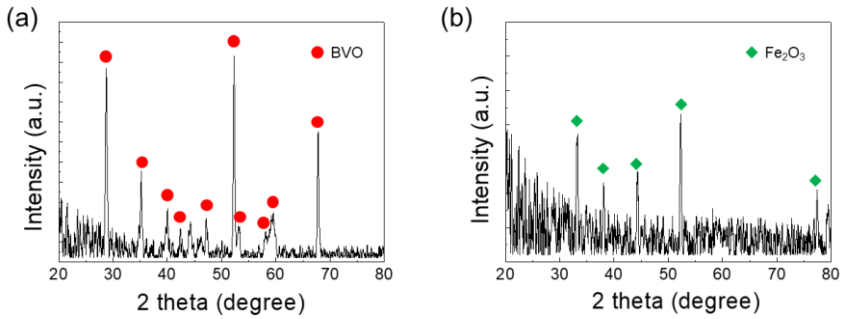

Figure 3.11 Grazing incidence X-ray diffaction of (a) BVO and (b) Fe_2O_3 on LAO/Nb:STO heterostructure.

Band offset manipulation with LAO interlayer can also be applied for other photoanode materials such as BVO and Fe_2O_3. 50 nm oxides (BVO and Fe_2O_3) films are deposited on Nb:STO with or without 3 uc LAO interlayer. Grazing incidence X-ray diffraction scans of BVO and Fe_2O_3 films are displayed in Figure 3.11. Water splitting property of BVO/LAO/Nb:STO is shown in Figure 3.12. Photocurrent of the heterostructure without LAO interlayer is comparable with that of bare Nb:STO,[49, 50] since electrons generated in BVO is blocked with Schottky barrier while electron-hole pairs generated in Nb:STO is effectively separated with upward bent Nb:STO energy band at the BVO/Nb:STO interface. Photocurrent in this case is rarely relying on the external bias. On the other hand, photocurrent of the heterostructure with LAO interlayer increases gradually as the external bias getting higher. Transient light illumination at 1.23 V vs RHE in Figure 3.12b shows that LAO interlayer boosts photocurrent of the heterostructure twice as much as the that of the heterostructure without LAO interlayer. EIS also reveals that BVO/LAO/Nb:STO has smaller semicircle, indicating that the charge transfer resistance of the heterostructure with LAO interlayer is smaller than that of the heterostructure without LAO interlayer. Energy

band diagram of the BVO/Nb:STO with or without LAO interlayer is depicted in Figure 3.12d. Internal electric field induced by the alternating polar sheets in LAO interlayer produces potential step at the BVO/Nb:STO hetero interface, leading to the Schottky barrier removal and turn the Schottky contact into Ohmic. Thus, the electrons generated in BVO can travel to Nb:STO substrate with assistant of LAO interlayer.

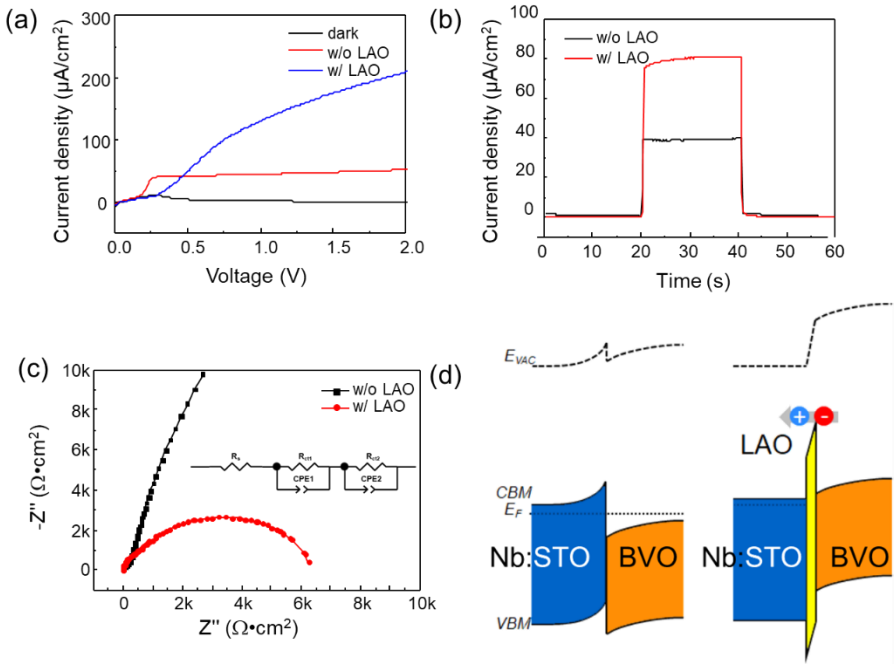

Figure 3.12 Photoelectrochemical properties of BVO / LAO / Nb:STO. (a) Linear sweep voltammetry. (b) Transient absorption spectroscopy. (c) Electrochemical impedence spectra. (d) Energy band diagram with or without LAO interlayer.

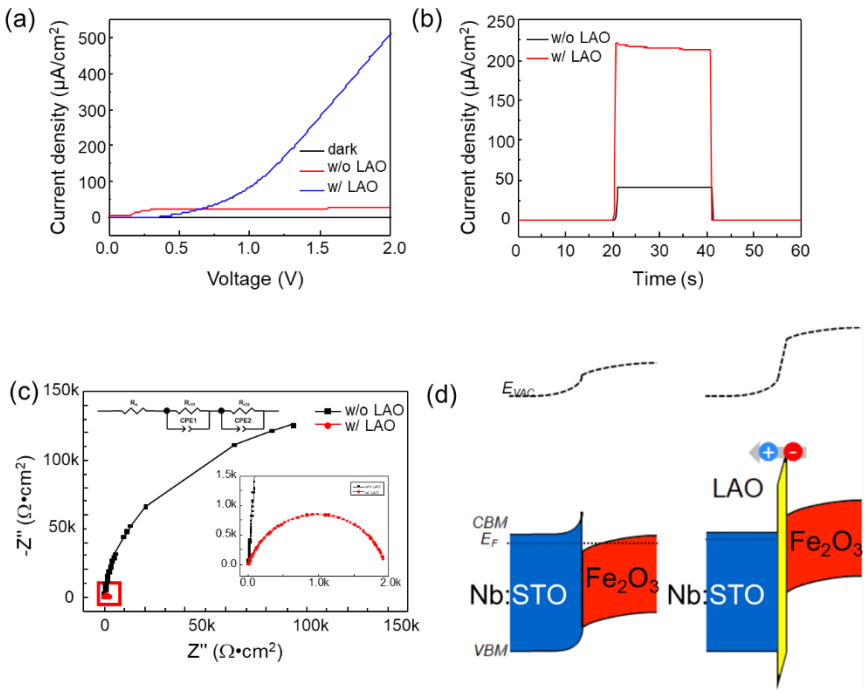

Figure 3.13 Photoelectrochemical properties of α-Fe_2O_3/LAO/Nb:STO heterostructure. (a) Linear sweep voltammetry. (b) Transient absorption spectroscopy. (c) Electrochemical impedence spectra. (d) Energy band diagram of the heterostructure with or without LAO interlayer.

In case of Fe_2O_3, linear sweep voltammetry curve without LAO interlayer shows the similar behavior of Nb:STO in the same reason with BVO/Nb:STO case. Photocurrent density of Fe_2O_3/LAO/Nb:STO is four times enhanced than Fe_2O_3/Nb:STO at 1.23 V vs RHE. EIS also reveals

that the charge transfer resistance is reduced with LAO interlayer. Energy band diagram of Fe_2O_3/Nb:STO with or without LAO interlayer is depicted in Figure 3.13d.

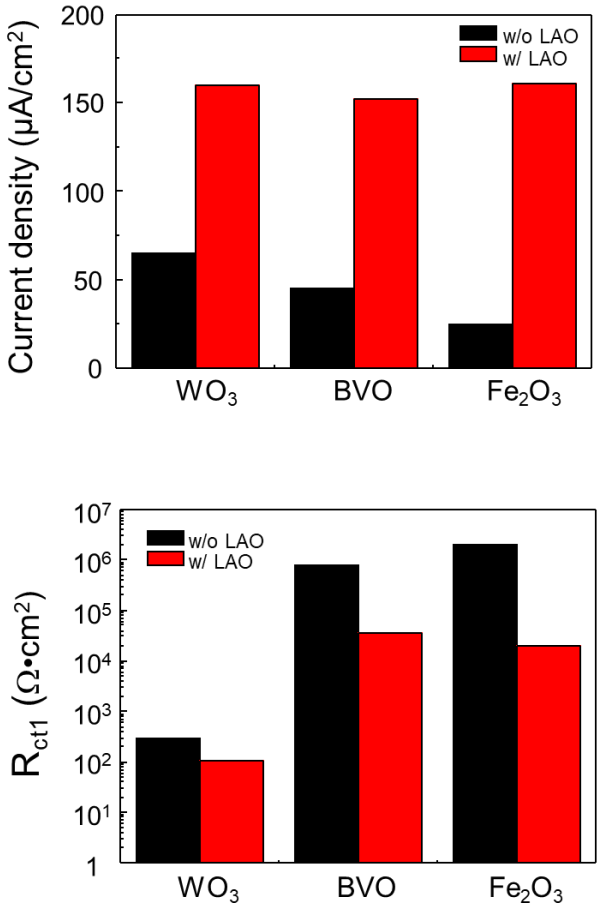

Figure 3.14 Comparison of photoelectrochemical properties. (a) Comparison of photocurrent densities with or without LAO interlayers at 1.23 V vs RHE. (b) Comparison of charge transfer resistances with or without LAO interlayers.

Water oxidation performance of oxide heterostructures are compared as shown in Figure 3.14. Photocurrent densities at 1.23 V vs RHE of all heterostructures is enhanced with LAO interlayer than the heterostructure without LAO interlayer. Interestingly, photocurrent density of α-Fe_2O_3/Nb:STO is only half of that of the BVO/Nb:STO heterostructure, even though they both shows the photoelectrochemical property of bare Nb:STO substrate. This is because of the different depletion width of Nb:STO substrate in each sample. Depletion width in Nb:STO substrate W_{STO} can be calculated by the following equation:

$$W_{STO} = \sqrt{\frac{2\varepsilon_{STO}\phi}{q}\left(\frac{N_{oxide}}{N_{STO}}\right)\left(\frac{1}{N_{oxide} + N_{STO}}\right)}$$

Where ε_{STO} is the dielectric constant of the STO substrate, ϕ is the work function difference, q is electron charge, N_{oxide} is the carrier concentrations of BVO and α-Fe_2O_3, and N_{STO} is the carrier concentration of Nb:STO.[51-54] The estimated depletion width of Nb:STO substrate attached with BVO is about 4 nm while Nb:STO attached with α-Fe_2O_3 is 2 nm, according to previous reported constants.

Consequently, photoelectrochemical reactivity of Nb:STO under BVO is twice as much as that of Nb:STO under α-Fe_2O_3. Charge transfer resistances shown in Figure 3.14b designate that LAO interlayer diminishes Schottky barrier and assist charge transfer between oxides.

These result shows the application potential of LAO interlayer to other oxide heterostructures that has Schottky barrier at the interface. With atomically thin LAO layer, band offset is modulated to have potential step with large internal electric field. This potential step enforces oppress Schottky barrier height and make Schottky contact Ohmic. Therefore, electrons can easily pass through the interface freely.

In summary, enhanced photoelectrochemical reaction of heterostructures with LAO interlayer attribute to band offset manipulation with internal electric field induced by polar sheets in LAO. 0.93 eV of potential step is produced with internal electric field. Charge transfer resistances are decreased with the electric field since Schottky barrier height is reduced or removed. Accordingly, electrons generated with sunlight in photoactive material can travel across the oxide heterointerface with LAO interlayer whereas electrons are restricted to go across the

heterointerface without LAO interlayer. Although LAO is a wide-gap insulator with 5.6 eV band gap, when deposited epitaxially in [001] direction with atomically thin thickness, LAO assist electron transfer in out of plane direction through tunneling. This would provide a new perception, idea, and deeper understanding for designing and controlling oxide heterointerfaces.

3.4. References

[1] Y. Park, K. J. McDonald, K.-S. Choi, *Chem. Soc. Rev.* **2013**, *42*, 2321.

[2] N. S. Lewis, D. G. Nocera, *Proc. Natl. Acad. Sci.* **2006**, *103*, 15729.

[3] M. G. Walter, E. L. Warren, J. R. McKone, S. W. Boettcher, Q. Mi, E. a Santori, N. S. Lewis, *Chem. Rev.* **2010**, *110*, 6446.

[4] B. Kumar, M. Llorente, J. Froehlich, T. Dang, A. Sathrum, C. P. Kubiak, *Annu. Rev. Phys. Chem.* **2012**, *63*, 541.

[5] A. J. Bard, M. A. Fox, *Acc. Chem. Res.* **1995**, *28*, 141.

[6] P. D. Tran, L. H. Wong, J. Barber, J. S. C. Loo, *Energy Environ. Sci.* **2012**, *5*, 5902.

[7] M. Grätzel, *Nature* **2001**, *414*, 338.

[8] A. Fujishima, K. Honda, *Nature* **1972**, *238*, 37.

[9] J. R. Bolton, *Sol. Energy* **1996**, *57*, 37.

[10] S. U. M. Khan, *J. Electrochem. Soc.* **1998**, *145*, 89.

[11] S. U. M. Khan, J. Akikusa, *J. Phys. Chem. B* **1999**, *103*, 7184.

[12] S. U. M. Khan, M. Al-Shahry, W. B. Ingler, *Science* **2002**, *297*, 2243.

[13] J. Akikusa, S. U. M. Khan, *Int. J. Hydrogen Energy* **2002**, *27*, 863.

[14] J. Song, J. Cha, M. G. Lee, H. W. Jeong, S. Seo, J. A. Yoo, T. L. Kim, J. Lee, H. No, D. H. Kim, S. Y. Jeong, H. An, B. H. Lee, C. W. Bark, H. Park, H. W. Jang, S. Lee, *J. Mater. Chem. A* **2017**, *5*, 18831.

[15] J. Song, T. L. Kim, J. Lee, S. Y. Cho, J. Cha, S. Y. Jeong, H. An, W. S. Kim, Y.-S. Jung, J. Park, G. Y. Jung, D.-Y. Kim, J. Y. Jo, S. D. Bu, H. W. Jang, S. Lee, *Nano Res.* **2018**, *11*, 642.

[16] F. Le Formal, N. Tétreault, M. Cornuz, T. Moehl, M. Grätzel, K. Sivula, *Chem. Sci.* **2011**, *2*, 737.

[17] J. H. Kim, J.-W. Jang, Y. H. Jo, F. F. Abdi, Y. H. Lee, R. van de Krol, J. S. Lee, *Nat. Commun.* **2016**, *7*, 13380.

[18] M. A. Henderson, *Surf. Sci. Rep.* **2011**, *66*, 185.

[19] H. Tong, S. Ouyang, Y. Bi, N. Umezawa, M. Oshikiri, J. H. Ye, *Adv. Mater.* **2012**, *24*, 229.

[20] H. Zhou, Y. Qu, T. Zeid, X. Duan, *Energy Environ. Sci.* **2012**, *5*, 6732.

[21] Y. Ma, X. Wang, Y. Jia, X. Chen, H. Han, C. Li, *Chem. Rev.* **2014**, *114*, 9987.

[22] G. Singh-Bhalla, C. Bell, J. Ravichandran, W. Siemons, Y. Hikita, S. Salahuddin, A. F. Hebard, H. Y. Hwang, R. Ramesh, *Nat. Phys.* **2011**, *7*, 80.

[23] I. Giaever, *Phys. Rev. Lett.* **1960**, *5*, 464.

[24] S. H. Lo, D. A. Buchanan, Y. Taur, W. Wang, *IEEE Electron Device Lett.* **1997**, *18*, 209.

[25] D. Dijkkamp, T. Venkatesan, X. D. Wu, S. A. Shaheen, N. Jisrawi, Y. H. Min-Lee, W. L. McLean, M. Croft, *Appl. Phys. Lett.* **1987**, *51*, 619.

[26] A. Ohtomo, H. Y. Hwang, *Nature* **2006**, *441*, 120.

[27] N. Reyren, S. Thiel, A. D. Caviglia, L. F. Kourkoutis, G. Hammerl, C. Richter, C. W. Schneider, T. Kopp, A.-S. Ruetschi,

D. Jaccard, M. Gabay, D. A. Muller, J.-M. Triscone, J. Mannhart, *Science* **2007**, *317*, 1196.

[28] A. Brinkman, M. Huijben, M. van Zalk, J. Huijben, U. Zeitler, J. C. Maan, W. G. van der Wiel, G. Rijnders, D. H. A. Blank, H. Hilgenkamp, *Nat. Mater.* **2007**, *6*, 493.

[29] B. Kalisky, J. a. Bert, B. B. Klopfer, C. Bell, H. K. Sato, M. Hosoda, Y. Hikita, H. Y. Hwang, K. a. Moler, *Nat. Commun.* **2012**, *3*, 922.

[30] J. A. Bert, B. Kalisky, C. Bell, M. Kim, Y. Hikita, H. Y. Hwang, K. a. Moler, *Nat. Phys.* **2011**, *7*, 767.

[31] C. W. Bark, D. a. Felker, Y. Wang, Y. Zhang, H. W. Jang, C. M. Folkman, J. W. Park, S. H. Baek, H. Zhou, D. D. Fong, X. Q. Pan, E. Y. Tsymbal, M. S. Rzchowski, C. B. Eom, *Proc. Natl. Acad. Sci.* **2011**, *108*, 4720.

[32] C. W. Bark, P. Sharma, Y. Wang, S. H. Baek, S. Lee, S. Ryu, C. M. Folkman, T. R. Paudel, a. Kumar, S. V. Kalinin, a. Sokolov, E. Y. Tsymbal, M. S. Rzchowski, a. Gruverman, C. B. Eom, *Nano Lett.* **2012**, *12*, 1765.

[33] T. Yajima, M. Minohara, C. Bell, H. Kumigashira, M. Oshima, H. Y. Hwang, Y. Hikita, *Nano Lett.* **2015**, *15*, 1622.

[34] E. Assmann, P. Blaha, R. Laskowski, K. Held, S. Okamoto, G. Sangiovanni, *Phys. Rev. Lett.* **2013**, *110*, 1.

[35] F. Le Formal, M. Grätzel, K. Sivula, *Adv. Funct. Mater.* **2010**, *20*, 1099.

[36] F. Le Formal, N. Tétreault, M. Cornuz, T. Moehl, M. Grätzel, K. Sivula, *Chem. Sci.* **2011**, *2*, 737.

[37] C. Sanchez, K. D. Sieber, G. A. Somorjai, *J. Electroanal. Chem.*

1988, *252*, 269.

[38] M. P. Dare-Edwards, J. B. Goodenough, A. Hamnett, P. R. Trevellick, *J. Chem. SOC. Faraday Trans. 1* **1983**, *79*, 2027.

[39] P. Iwanski, *J. Electrochem. Soc.* **1981**, *128*, 2128.

[40] G. Horowitz, *J. Electroanal. Chem.* **1983**, *159*, 421.

[41] T. W. Hickmott, *J. Appl. Phys.* **2000**, *87*, 7903.

[42] R. G. Forbes, *Vac. Microelectron. Conf. 1998. Elev. Int.* **1998**, *526*, 3.

[43] M. Lenzlinger, E. H. Snow, *J. Appl. Phys.* **1969**, *40*, 278.

[44] Z. Q. Liu, C. J. Li, W. M. Lü, X. H. Huang, Z. Huang, S. W. Zeng, X. P. Qiu, L. S. Huang, A. Annadi, J. S. Chen, J. M. D. Coey, T. Venkatesan, Ariando, *Phys. Rev. X* **2013**, *3*, 021010.

[45] Y. Hikita, K. Nishio, L. C. Seitz, P. Chakthranont, T. Tachikawa, T. F. Jaramillo, H. Y. Hwang, *Adv. Energy Mater.* **2016**, *6*, 1.

[46] S. Thiel, G. Hammerl, A. Schmehl, C. W. Schneider, J. Mannhart, *Science* **2006**, *313*, 1942.

[47] W. Siemons, G. Koster, H. Yamamoto, W. A. Harrison, G. Lucovsky, T. H. Geballe, D. H. A. Blank, M. R. Beasley, *Phys. Rev. Lett.* **2007**, *98*, 3.

[48] U. Treske, N. Heming, M. Knupfer, B. Büchner, E. Di Gennaro, A. Khare, U. Scotti Di Uccio, F. Miletto Granozio, S. Krause, A. Koitzsch, *Sci. Rep.* **2015**, *5*, 1.

[49] Y. Ham, T. Minegishi, T. Hisatomi, K. Domen, *Chem. Commun.* **2016**, *52*, 5011.

[50] A. N. Pinheiro, E. G. S. Firmiano, A. C. Rabelo, C. J. Dalmaschio, E. R. Leite, *RSC Adv.* **2014**, *4*, 2029.

[51] K. G. Rana, V. Khikhlovskyi, T. Banerjee, *Appl. Phys. Lett.* **2012**, *100*, 1.

[52] S. Sarkar, N. S. Das, K. K. Chattopadhyay, *Solid State Sci.* **2014**, *33*, 58.

[53] S. S. Shinde, R. A. Bansode, C. H. Bhosale, K. Y. Rajpure, *J. Semicond.* **2011**, *32*, 013001.

[54] K. A. Müller, H. Burkard, *Phys. Rev. B* **1979**, *19*, 3593.

4. Enhancing water splitting performance with sequential type-II junctions produced by $Fe_2O_3/BiVO_4/WO_3$ oxide ternary structure

4.1. Introduction

Photoelectrochemical water oxidation reaction involves multiple steps including electron-hole pair generation with absorbed light, charge separation and transportation, and charge transfer to water.[1-4] TiO_2 has been intensively studied since after the discovery of the water splitting property in 1972. However, TiO_2 has theoretical limitation in solar energy conversion efficiency of 5% due to the large band gap (3.2 eV), which inhibit practical applications. As an alternative, numerous n-type semiconductors have been studied that has properly small band gap, sufficiently long carrier life time, and good charge separation efficiency.[5-9] Among various materials, WO_3, BVO, and Fe_2O_3 are representative photoactive material with higher conversion efficiencies of 5.8%, 9.2% and 15.5%, respectively, as shown in Figure 4.1.[10] Nevertheless, none of the research has reached the theoretical maximum

conversion efficiency because of excessive electron-hole pair recombination, slow charge transportation in material, and poor water oxidation kinetics. Therefore, many attempts have been made to overcome the drawbacks such as morphology modification, doping, plasmonic effect utilization, co-catalyst loading, and others.

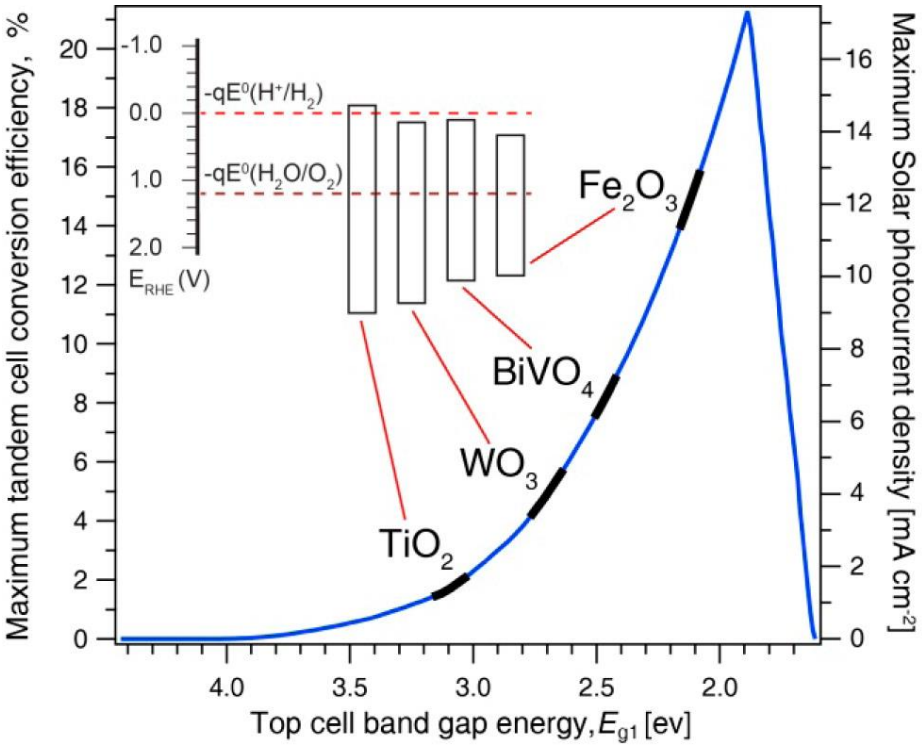

Figure 4.1 Theoretical maximum solar-to-hydrogen conversion efficiency and photocurrent density vs band gap energy of photoactive materials.[10]

4.1.1. Various strategies for enhanced water oxidation performance

Morphology control

Carrier harvesting width which is the summation of depletion width and minority carrier diffusion length in oxide materials are generally very small (*e.g.* 10 nm in Fe_2O_3).[11] Since nanosize materials possess large surface-to-volume ratio, abundant surface states, and various reaction sites,[2] nanostructuring is one of the most viable attempts for overcome small carrier harvesting width.[12] When the size of photoactive material reduced, photogenerated electrons would be easier to be transported to the bottom electrode, leading to the increase of hole lifetime and rise photoreactivity of the material.[13] Nanoporous photoelectrode consist of nanoparticles smaller than its hole diffusion length would have enhanced water oxidation performance with reduced recombination rate since holes are consumed by oxidizing water.[14]

Doping

Doping also can assist energy band control, light absorption, and charge

transfer. The addition of trace amount of dopants can also significantly change the electrical and optical properties of photoactive materials. It is also possible to change the energy band structure and position with doping. Some n-type dopant such as Si, Sn, and Ge in Fe_2O_3 improves charge transport in the matrix with the domination of extra one electron per every dopant atom, leading to the enhanced water splitting performance.[15] Meanwhile, W doping in BVO not only induces conductivity enhancement, but also improves charge separation efficiency with band bending. Since W raises Fermi level in BVO, heterostructure with 10-step gradient doping of W result in the energy band bending over the entire photoanode as shown in Figure 4.2d.[16]

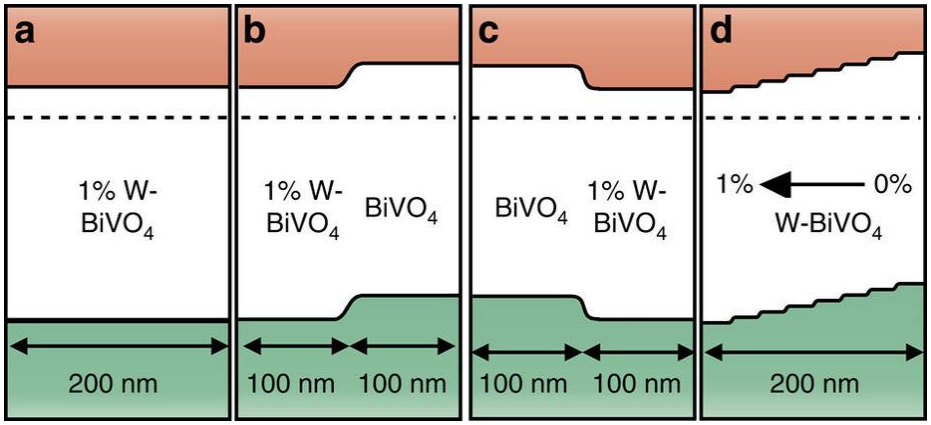

Figure 4.2 Schematic energy band diagram of BVO samples.[16]

Plasmonic effect utilization

Plasmonic effect in metal nanoparticles are reported to overcome the limitations in photoanode. In general, Au and Ag nanoparticles are used for water oxidation because of their chemical stability, formation of Schottky junction, and localized surface plasmon resonance (LSPR) with visible light. The formation of Schottky junction modifies the electronic band structure, leading to the enhanced charge separation.[17] LSPR also possesses several advantages;[18-22] Firstly, the plasmon resonant energy transfer effect can generate field-enhanced electron-hole pair near the surface. Secondly, plasmon-induced direct electron transfer creates additional charge carriers and inject the hot electrons into the conduction band of the photoelectrode material. Finally, resonant photon scattering of metal nanoparticles increases the average photon path-length. Au and Ag nanoparticles also can reduce the recombination rate with strong surface plasmon resonance.

Co-catalyst loading

One of the biggest limitation of water oxidation is poor surface catalytic

reaction with slow kinetics. Thus, various type of catalysts such as NiOOH, FeOOH, cobalt phosphate (Co-Pi) and CoO_x have been tested to enhance water oxidation property. Water oxidation process with CoO_x is known to be rapid and reduced recombination rates since Co^{2+} fill surface traps which react as electron-hole recombination sites.[23] A Co^{2+} monolayer can result in the onset potential reduction of 0.1 V.[24] Co-Pi also has been reported to enhance the performance of WO_3, BVO, and Fe_2O_3.[25-28] In these cases, the thicknesses of the CoO_x and Co-Pi are critical for the performance. In addition, loading NiO on the surface of the photoactive material also enhances water splitting performance. NiO would turn into hydroxyl-ion permeable NiOOH during the water oxidation reaction, leading to the formation of buried p-n junction since NiO and NiOOH are p-type materials.

4.1.2. Heterostructured photoelectrodes

Heterostructure which is the combination of two different materials is usually made to possesses all merits of the materials while suppresses disadvantages. Band structure of a heterostructure can have three

different lineups: type I straddling lineup, type II staggered lineup, and type III broken gap lineup (Figure 4.3).[29] Among these lineups, type II junction give rise to the enhancement of photogenerated electron-hole separation. Thus, various combinations that makes type II junction have been studied for improved water oxidation performance.[30-32]

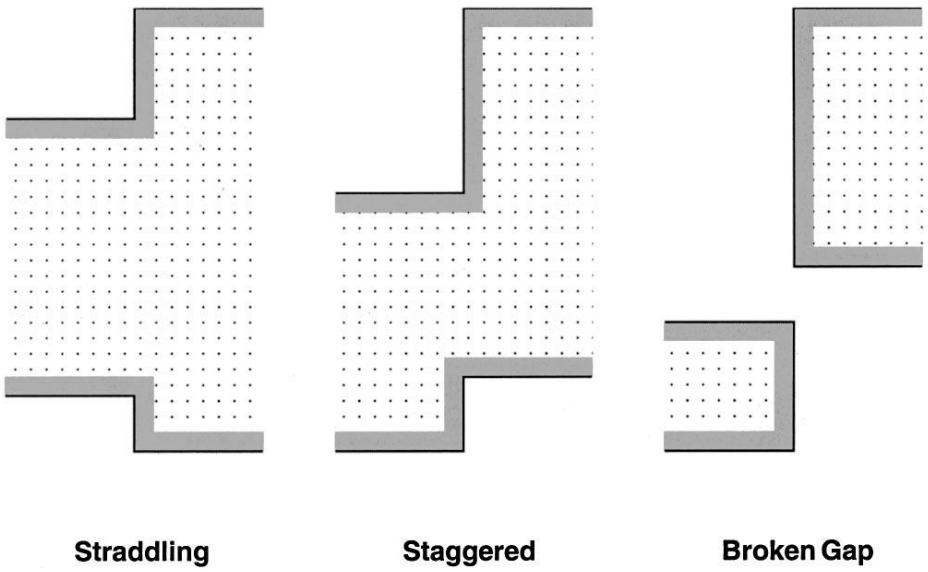

Figure 4.3 Three different band lineups of heterostructures.[29]

4.1.3. Motivation and objectives

The motivation and objectives of this chapter is to construct

heterostructured photoanode that combines the merits of each material while suppressing the demerits. As an n-type photoanode, although WO_3 is stable in aqueous solution, good light absorber, and earth abundant material, theoretical solar-to-hydrogen conversion efficiency is limited up to 4.5 % since the band gap of WO_3 is wide as 2.7 eV. BVO also receiving attention with its stability, maximum 9.2% energy conversion, and cheap production price, but poor surface charge transfer reaction limits the exploitation of its full potential. Fe_2O_3 has advantages such as stable in water and good charge transfer efficiency. However, for practical use, a high requisite overpotential for water oxidation, low absorption coefficient requiring ~500 nm thick films for complete sunlight absorption, poor majority carrier transport, and a short diffusion length of minority carriers, ~5 nm limits for Fe_2O_3 to be used. Although aforementioned three materials are promising candidates for photoanode, none of them can be used practically without combining with each other. When the heterostructure is constructed with each other, enhanced light absorption with multiple band gaps, improved charge separation with intrinsically bent energy band at the interface, and reduced charge recombination rate are expected.

WO_3 and BVO have been most frequently coupled in order to enhance light absorption and charge separation. Electrons generated in BVO would be migrated and join electrons generated in WO_3 layer to be transferred to the bottom electrode. Holes, on the other hand, would be moved to BVO and oxide/electrolyte interface since the valence band maximum of BVO is located higher than that of WO_3. Consequently, this type II junction improves charge separation and water oxidation performance. In the same context, sequential type II junction with three layered heterostructure composed of WO_3, BVO, and Fe_2O_3, which is not reported yet, would further enhance the photoelectrochemical reaction for water oxidation. In this chapter, Fe_2O_3/BVO/WO_3 heterostructure is constructed to unlock the full potential of each material. Sequential type II junction is constructed with ternary layers observed by X-ray photoemission spectroscopy (XPS) and UV-Visible spectroscopy. Water oxidation property confirmed by photocurrent density is also enhanced with ternary structure. However, when the Fe_2O_3 cover layer is thick as 100 nm, the performance degraded resulted from the reverse type II junction at the Fe_2O_3/BVO interface. This provides insight of fabricating high performance photoelectrode.

4.2. Experimental method

4.2.1. Target preparation

WO_3, BVO, and Fe_2O_3 targets are prepared as described in Chapter 3.2.1.

4.2.2. Film growth by pulsed laser deposition method

WO_3 film is firstly grown on surface cleaned F-doped tin oxide (FTO) with pulsed laser deposition method under oxygen pressure of 300 mTorr, substrate temperature of 500 ℃ repetition rate of 3 Hz, and laser density of 2.23 J/cm^2. Secondly, BVO is deposited on WO_3 surface at 330 ℃, under oxygen pressure of 300 mTorr, laser density of 1.62 J/cm^2, and repetition rate of 3 Hz. Fe_2O_3 film is deposited lastly on the surface under 100 mTorr oxygen pressure, equal temperature with BVO growth, laser density of 2 J/cm^2, and repetition rate of 2 Hz.

4.2.3. Analysis methods

Water splitting performance is measured as described in Chapter 3.2.4 with back-side illumination.

4.3. Result and discussion

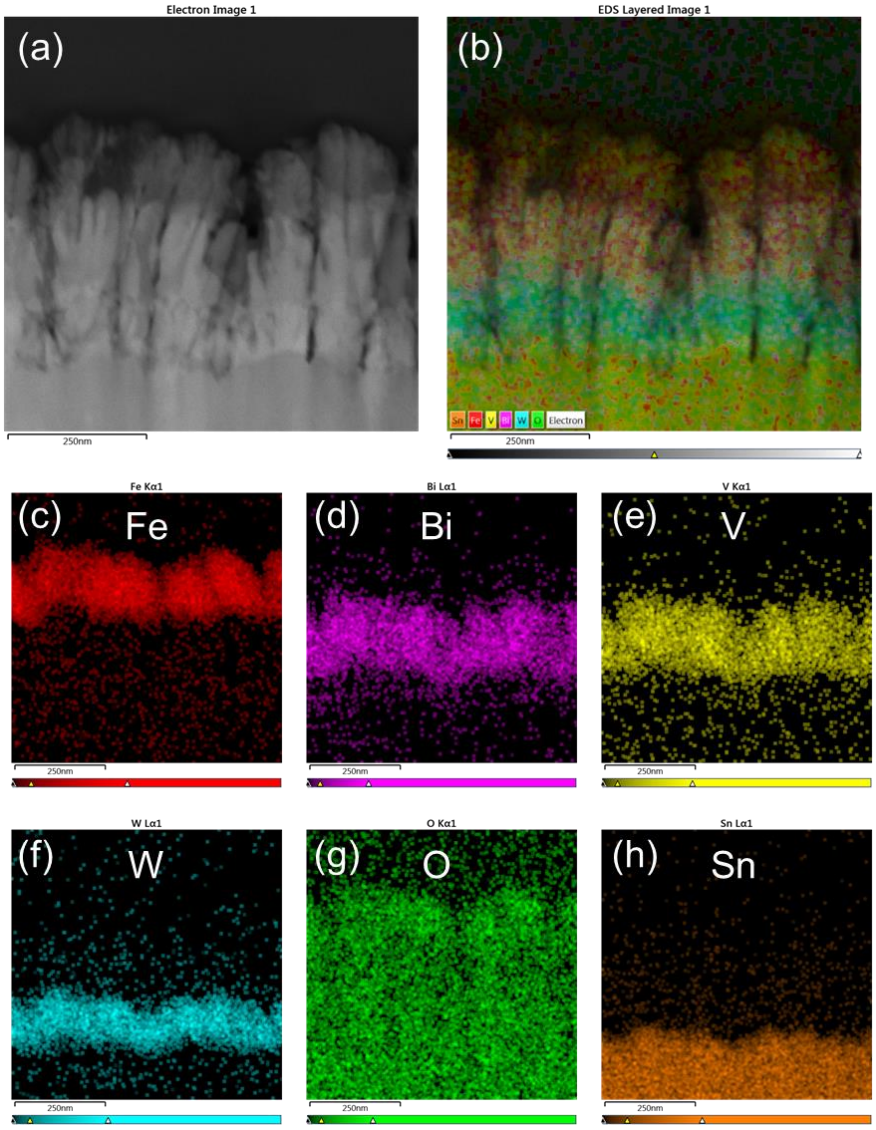

Figure 4.4 (a) HAADF STEM image of 100 nm Fe_2O_3/200 nm BVO/100 nm WO_3 structure. (b) EDS image of (a). (c-h) EDS mapping of each element.

Four samples (WO_3. BVO/WO_3, 10 nm Fe_2O_3/ BVO/WO_3, and 100 nm Fe_2O_3/ BVO/WO_3) were prepared on FTO with pulsed laser deposition method. Among four samples, HAADF STEM image of 100 nm Fe_2O_3/BVO/WO_3 is displayed Figure 4.4. EDS mapping of the image reveals that the thicknesses of WO_3, BVO, and Fe_2O_3 are 100 nm, 250 nm, and 100 nm respectively.

Photoelectrochemical properties of four samples are measured under AM 1.5G sunlight illumination as shown in Figure 4.5. Linear sweep voltammetry curves indicate that BVO/WO_3 heterostructure has enhanced water oxidation performance than WO_3 photoanode and the sample with 10 nm Fe_2O_3 top layer over BVO/WO_3 has the best water oxidizing ability. On the other hand, the sample with thick Fe_2O_3 top layer has decreased water oxidizing property. This can be also confirmed in EIS plot. EIS is measured at 1.23 V vs RHE under sunlight. Equivalent circuits are displayed as an inset figure of Figure 4.5b. The circuit is consisting of series resistance governing all resistances among photoanodes, and charge transfer resistance at the oxide/electrolyte interface. Resistances are compared in Table 4.1. Series resistance is all similar in all samples. Charge transfer resistance of WO_3 is the largest,

indicating the poor charge transfer kinetics of WO_3 to water. R_{ct} in BVO/WO_3 and 10 nm $Fe_2O_3/BVO/WO_3$ is similar while R_{ct} in 100 nm $Fe_2O_3/BVO/WO_3$ is larger than those two heterostructures. This means that the enhanced photocurrent density is not originated from the charge transfer but originated from other effect since the charge transfer kinetics in BVO/WO_3 and 10 nm $Fe_2O_3/BVO/WO_3$ heterostructures are similar. To determine the carrier density and capacitance of electrical double layer at the oxide/electrolyte interface, Mott-Schottky plot is measured. The carrier density (N_D) can be calculated with the following equation:

$$N_D = \frac{2}{e\varepsilon\varepsilon_0}\left(\frac{d(1/C^2)}{dV}\right)^{-1}$$

Where e is electron charge, ε is dielectric constant of the material, ε_0 is permittivity of vacuum, and V is applied bias. This equation shows that the slope of the Mott-Schottky plot is inverse proportional to the carrier density. WO_3 and 100 nm $Fe_2O_3/BVO/WO_3$ has the similarly high slope of Mott-Schottky plot, indicating that the carrier concentration is relatively low whereas 10 nm $Fe_2O_3/BVO/WO_3$ heterostructure has the lowest slope and highest carrier concentration. Thus, enhanced water splitting property is initiated from the high carrier density.

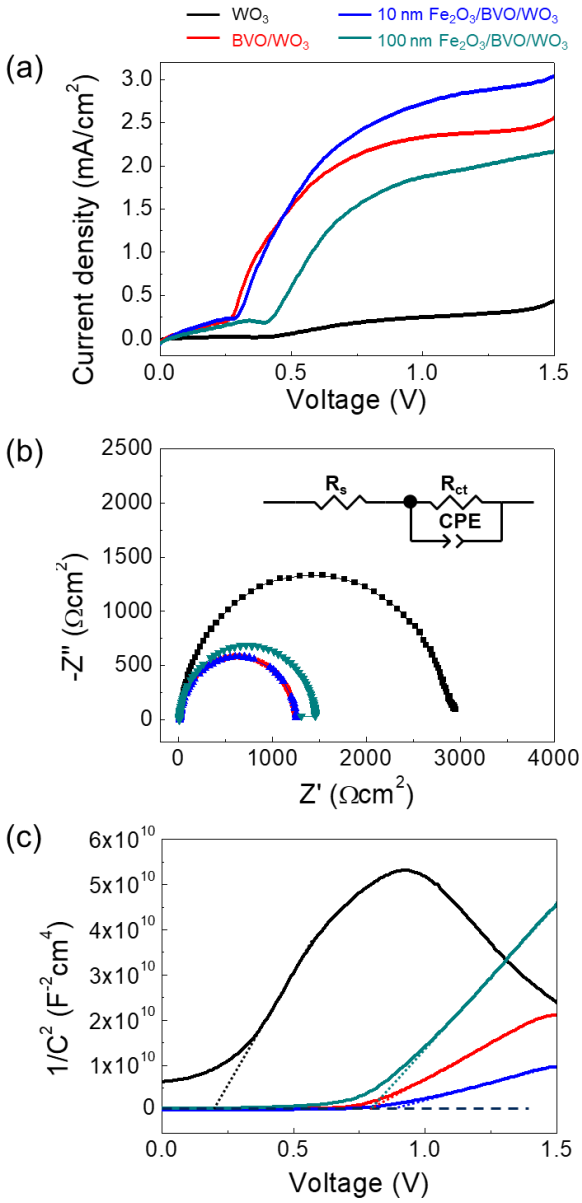

Figure 4.5 Photoelectrochemical properties of samples. (a) Linear sweep voltammetry, (b) EIS curves, and (c) Mott-Schottky plot of WO_3, BVO/WO_3, and $Fe_2O_3/BVO/WO_3$

Table 4.1 Series resistance (R_s) and charge transfer resistance (R_{ct}) across interfaces.

Structure	R_s [Ω cm^2]	R_{ct} [Ω cm^2]
WO_3	15.5	2885
BVO/WO_3	10.4	1238
10 nm Fe_2O_3/BVO/WO_3	11.5	1245
100 nm Fe_2O_3/BVO .WO_3	6.9	1437

The difference of carrier concentration in different samples would be the result of different carrier harvesting width which can be defined by the summation of depletion width and minority carrier diffusion length. Thus, confirming the energy band diagram in each sample is indispensable. XPS and UV-Vis are displayed in Figure 4.6. XPS indicates the difference between Fermi level valence band maximum and UV-Vis plot reveals the energy band gap. Deduced energy band diagram of the two three-layered heterostructures based on the Figure 4.6 is depicted in Figure 4.7. When the thickness of Fe_2O_3 overlayer is thin, the three-layered heterostructure has sequential type II junction. Electron-hole pair would be separated not only in the BVO/WO_3 interface but also in the

Fe_2O_3/BVO interface, which would result in the enhanced charge separation and the reduction of recombination rate. However, when the thickness of Fe_2O_3 overlayer is thick, since the Fe_2O_3 is n-type material, reverse type II junction is formed at the Fe_2O_3/BVO interface, leading to the reduction of photocurrent. This reverse type II junction would block some holes to be transferred to the oxide/electrolyte interface, and thus the photocurrent density decreased. Still, the valence band maximum of the Fe_2O_3 is higher than that of WO_3. Thus, water splitting performance is higher than WO_3 sample.

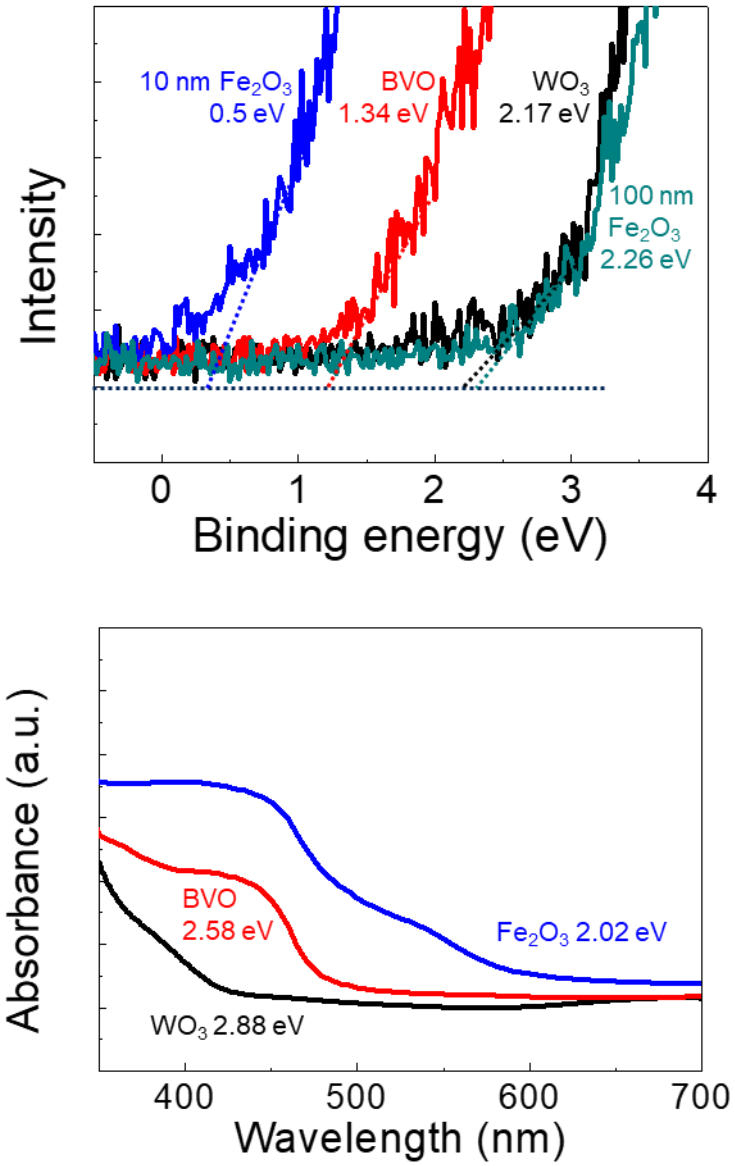

Figure 4.6 XPS (upper) and UV-Vis (lower) scan of samples.

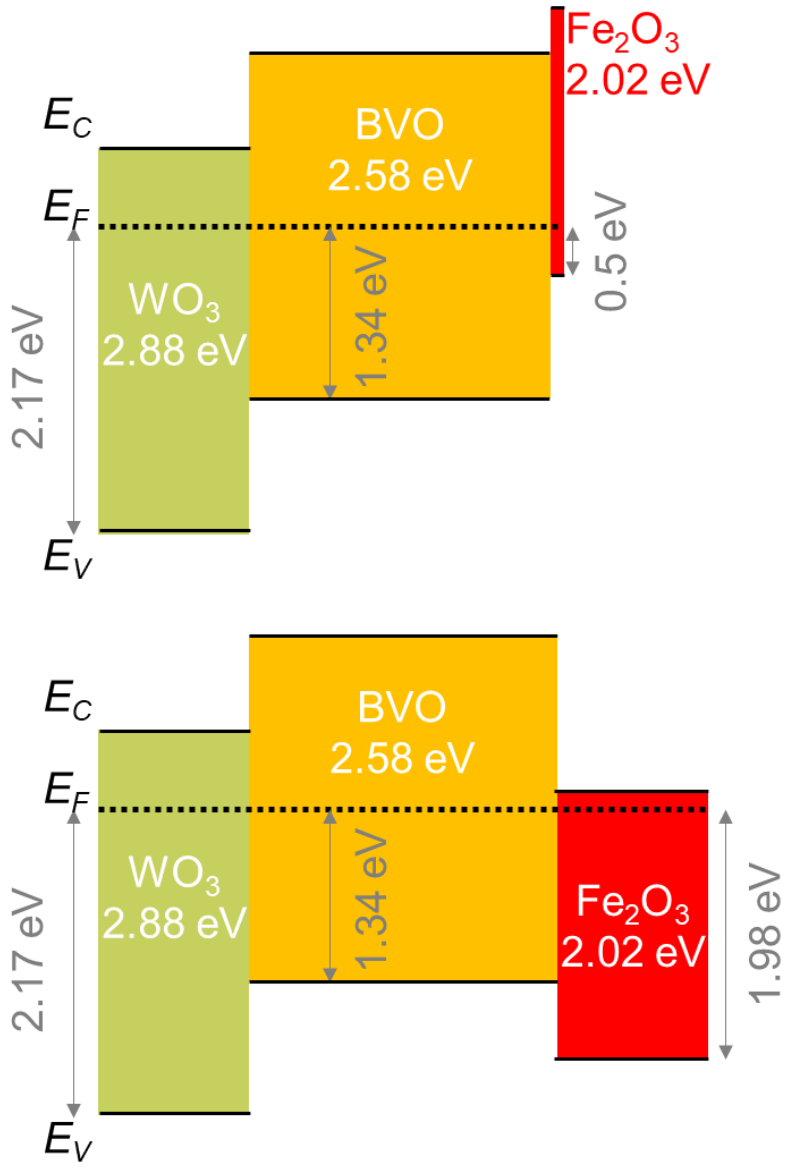

Figure 4.7 Energy band diagram based of (a) 10 nm Fe_2O_3/BVO/WO_3 and (b) 100 nm Fe_2O_3/BVO/WO_3.

IPCE spectra and photocurrents of the heterostructures containing BVO layer is measured both with front illumination and back illumination under 0.6 V vs RHE. In all cases, back illumination shows superior efficiencies and front illumination shows inferior conversion efficiencies. This is due to band alignment and the short carrier diffusion length in oxides. With back illuminations, UV light is absorbed in WO_3 region and visible light passes through WO_3 is absorbed in BVO and Fe_2O_3. Electrons generated in WO_3 is close to the back contact and holes generated in BVO is close to the electrolyte in BVO/WO_3 case. Thus, higher photocurrent is observed with back illumination. On the other hand, with front illumination, all light is absorbed in the surface oxide, hence the electrons generated in the surface layer is too far to be transferred to the bottom electrode. Especially in case of the three-layered film with 100 nm Fe_2O_3 top layer with front illumination, large amount of light would be absorbed in Fe_2O_3 and BVO, then the carriers will be separated reversely with inverse type II junction; electrons to the surface and holes to the WO_3 side, leading to the significantly reduced photocurrent and conversion efficiency.

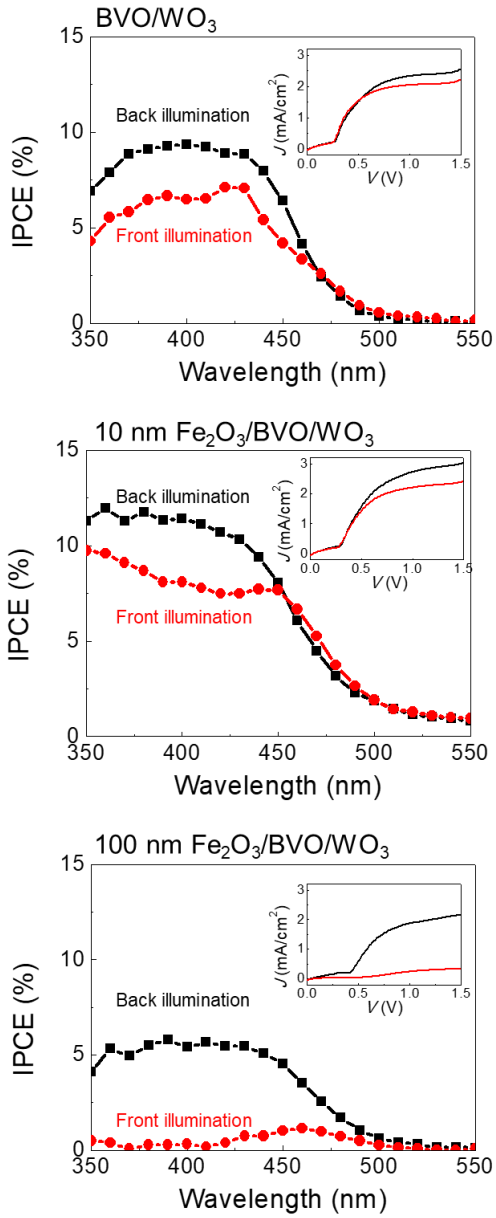

Figure 4.8 IPCE curves of samples with front and back illumination.

In summary, water splitting performance of four different samples, WO_3, BVO/WO_3, 10 nm- and 100 nm-Fe_2O_3/BVO/WO_3, are examined. Enhanced water oxidation ability is confirmed with three-layered structure with thin Fe_2O_3 layer thickness. The enhancement is due to the high carrier concentration which is originated from the enlarged carrier harvesting width with sequential type II junction. Interestingly, when the Fe_2O_3 layer is thick as 100 nm, reverse type II junction is formed at the heterointerface between Fe_2O_3 and BVO, leading to the reduction of water oxidation property. Therefore, constructing the oxide heterostructure with proper thickness and proper sequence are important for enhanced water splitting photoanode. This results provide insights to design water splitting photoelectrode for practical use.

4.4. References

[1] M. A. Henderson, *Surf. Sci. Rep.* **2011**, *66*, 185.

[2] H. Tong, S. Ouyang, Y. Bi, N. Umezawa, M. Oshikiri, J. H. Ye, *Adv. Mater.* **2012**, *24*, 229.

[3] H. Zhou, Y. Qu, T. Zeid, X. Duan, *Energy Environ. Sci.* **2012**, *5*, 6732.

[4] Y. Ma, X. Wang, Y. Jia, X. Chen, H. Han, C. Li, *Chem. Rev.* **2014**, *114*, 9987.

[5] S. U. M. Khan, J. Akikusa, *J. Phys. Chem. B* **1999**, *103*, 7184.

[6] J. Song, J. Cha, M. G. Lee, H. W. Jeong, S. Seo, J. A. Yoo, T. L. Kim, J. Lee, H. No, D. H. Kim, S. Y. Jeong, H. An, B. H. Lee, C. W. Bark, H. Park, H. W. Jang, S. Lee, *J. Mater. Chem. A* **2017**, *5*, 18831.

[7] J. Song, T. L. Kim, J. Lee, S. Y. Cho, J. Cha, S. Y. Jeong, H. An, W. S. Kim, Y. S. Jung, J. Park, G. Y. Jung, D. Y. Kim, J. Y. Jo, S. D. Bu, H. W. Jang, S. Lee, *Nano Res.* **2017**, 1.

[8] M. W. Kanan, D. G. Nocera, *Science* **2008**, *321*, 1072.

[9] Z. Zou, J. Ye, K. Sayama, H. Arakawa, *Nature* **2001**, *414*, 625.

[10] M. S. Prévot, K. Sivula, *J. Phys. Chem. C* **2013**, *117*, 17879.

[11] K. Sivula, F. Le Formal, M. Grätzel, *ChemSusChem* **2011**, *4*, 432.

[12] P. V. Kamat, *J. Phys. Chem. C* **2007**, *111*, 2834.

[13] S. Y. Jeong, K. S. Choi, H. M. Shin, T. L. Kim, J. Song, S. Yoon, H. W. Jang, M. H. Yoon, C. Jeon, J. Lee, S. Lee, *ACS Appl. Mater. Interfaces* **2017**, *9*, 505.

[14] T. W. Kim, K.-S. Choi, *Science* **2014**, *343*, 990.

[15] J. H. Kennedy, M. Anderman, R. Shinar, *J. Electrochem. Soc.* **1981**, *128*, 2371.

[16] F. F. Abdi, L. Han, A. H. M. Smets, M. Zeman, B. Dam, R. van de Krol, *Nat. Commun.* **2013**, *4*, 2195.

[17] J. Li, S. K. Cushing, P. Zheng, F. Meng, D. Chu, N. Wu, *Nat. Commun.* **2013**, *4*, 1.

[18] M. G. Lee, C. W. Moon, H. Park, W. Sohn, S. B. Kang, S. Lee, K. J. Choi, H. W. Jang, *Small* **2017**, *13*, 1701644.

[19] L. Zhang, L. O. Herrmann, J. J. Baumberg, *Sci. Rep.* **2015**, *5*, 1.

[20] S. Linic, P. Christopher, D. B. Ingram, *Nat. Mater.* **2011**, *10*, 911.

[21] M. Valenti, M. P. Jonsson, G. Biskos, A. Schmidt-Ott, W. A. Smith, *J. Mater. Chem. A* **2016**, *4*, 17891.

[22] F. F. Abdi, A. Dabirian, B. Dam, R. van de Krol, *Phys. Chem. Chem. Phys.* **2014**, *16*, 15272.

[23] B. S. Brunschwig, M. H. Chou, C. Creutz, P. Ghosh, N. Sutin, *J. Am. Chem. Soc.* **1983**, *105*, 4832.

[24] A. Kay, I. Cesar, M. Grätzel, *J. Am. Chem. Soc.* **2006**, *128*, 15714.

[25] M. W. Kanan, D. G. Nocera, *Science* **2008**, *321*, 1072.

[26] D. K. Zhong, D. R. Gamelin, *J. Am. Chem. Soc.* **2010**, *132*, 4202.

[27] K. J. McDonald, K.-S. Choi, *Energy Environ. Sci.* **2012**, *5*, 8553.

[28] D. K. Zhong, M. Cornuz, K. Sivula, M. Grätzel, D. R. Gamelin, *Energy Environ. Sci.* **2011**, *4*, 1759.

[29] H. Kroemer, *Rev. Mod. Phys.* **2001**, *73*, 783.

[30] W. Zhao, Y. Wang, Y. Yang, J. Tang, Y. Yang, *Appl. Catal. B Environ.* **2012**, *115–116*, 90.

[31] R. Saito, Y. Miseki, K. Sayama, *Chem. Commun.* **2012**, *48*, 3833.

[32] P. Ju, P. Wang, B. Li, H. Fan, S. Ai, D. Zhang, Y. Wang, *Chem. Eng. J.* **2014**, *236*, 430.

5. Conclusion

In this study, lateral and vertical charge transport in oxide heterostructure are investigated. New strategies to manipulate lateral and vertical charge transport are suggested. Control of electron conduction path and energy band diagram result in the variation of conductivity. Detailed explanations are as followings.

2DEG conductivity control with epitaxial strain

2DEG conductivity at LAO/STO heterointerface is tuned with the insertion of CTO interlayer that has intrinsic TiO_6 octahedral tilt. Interestingly, TiO_6 distortion is also observed with the epitaxial strain. Both tilt and distortion affect 2DEG conductivity as orbital overlap is influenced with tilt and distortion. Carriers are fluent at the LAO/CTO interface as confirmed with EELS, however, those carriers are immobile with distorted and tilted TiO_6 octahedrons. Observed tilting angle is about 145° which is smaller than the predicted 153.5°. O-Ti-O angle

which indicates the degree of TiO_6 distortion is also about 145°, smaller than the ideal value, 180°. Thus, TiO_6 octahedral tilt and distortion induced by epitaxial strain demonstrates a promising potential for applications with tuning the conductivity of the device.

Band offset tailoring with electrical dipole moment

Band offset is tailored with the insertion of atomically thin polar insulating LAO interlayer. The dipole moment of LAO interlayer reduced or removed Schottky barrier which was formed between WO_3 and Nb:STO and turned the contact into Ohmic. Two charge transfer dynamics of WO_3/LAO/Nb:STO heterostructure depending on the external bias are suggested: direct tunnelling and FN tunnelling. Direct tunnelling is dominant when applied external voltage is lower than 1 V while FN tunnelling become prominent with higher voltage. Potential applications for other heterointerfaces is shown by establishing BVO/LAO/Nb:STO and Fe_2O_3/ LAO/Nb:STO heterostructures. The result that shows photoelectrochemical and electrochemical properties of LAO inserted heterostructures can be significantly altered by the internal

electric field which is induced by the dipole of LAO interlayer provides new perception and a deeper understanding for controlling and designing oxide heterointerfaces,

Enhancing water splitting performance with sequential type-II junctions

Water splitting performance of ternary heterostructure is examined. Enhanced water oxidation ability is confirmed with three-layered structure with thin Fe_2O_3 layer thickness. The enhancement is due to the high carrier concentration which is originated from the enlarged carrier harvesting width with sequential type II junction. Interestingly, when the Fe_2O_3 layer is thick as 100 nm, reverse type II junction is formed at the heterointerface between Fe_2O_3 and BVO, leading to the reduction of water oxidation property. Therefore, constructing the oxide heterostructure with proper thickness and proper sequence are important for enhanced water splitting photoanode. This results provide insights to design water splitting photoelectrode for practical use.

For practical use of oxide heterostructures and miniaturization of electronic devices, controlling conductivity of the device is indispensable. In this point of view, this study provides deep insight to design practically usable electronic devices.

Abstract (in Korean)

2차원 전자가스와 물분해 광양극에 사용되는 산화물 이종접합 계면의 구조 및 전기적 특성 연구

이종 접합 계면은 소자 그 자체라고 불릴 정도로 소자의 구성에서 서로 다른 물질들의 접합 계면은 중요하다. 특히, 전자기기를 구성하는 소자들은 전하의 이동을 제어할 수 있어야 비로소 원하는 특성을 나타낼 수 있기 때문에 이종 접합을 통한 전도도 제어는 반도체 소자 제조의 핵심 기술 중 하나라 할 수 있다.

산화물 복합재료는 high-k 유전체, 고온 초전도성 우수한 강유전성 등, 다양한 물리적 현상으로 인해 중요한 물질로 여겨지고 있으며 많은 소자에 응용되어 사용되고 있다. 특히 최근 기술발전에 힘입어 원자 단위 증착이 가능해짐에 따라 자연계의 벌크 재료에서는 발견되지 않던 특이한 성질들이 발견되고 이에 대한 응용 연구가 활발히 진행되고 있다.

본 논문에서는 산화물 복합재료의 이종 접합 계면에서 발생하는 특이한 현상들을 이용해 수평 및 수직방향의 전하 이동을 제어하고 그 응용 가능성을 제시하였다. 이를 위해 크게 세 가지 연구를 진행하였는데, 이는 다음과 같다.

첫 째는 산화물에서의 2차원 전자 가스의 수평방향 이동 제어 연구이다. $SrTiO_3$ 와 $LaAlO_3$ 사이 계면에서 형성되는 2차원 전자 가스의 형성이 보고된 바 있고, 이 2차원 전자 가스는 $SrTiO_3$ 기판 내 TiO_6 팔면체의 기울어진 정도에 따라 전도성이 변하는 특징이 있다. $CaTiO_3$ 물질은 이 팔면체가 기울어져 있어 $CaTiO_3$를 $LaAlO_3$와 $SrTiO_3$ 사이 계면에 삽입함으로써 계면 사이에 형성되는 2차원 전자 가스의 전도도를 제어할 수 있음을 보였을 뿐만 아니라, $CaTiO_3$ 내의 TiO_6 팔면체의 뒤틀림 또한 발견하였다.

둘 째로는 밴드 오프셋 변화를 통한 수직방향 전하 이동 제어 연구이다. $LaAlO_3$는 큰 쌍극자 모멘트를 갖는 물질로써 이 모멘트가 유발하는 내재적인 전기장을 활용하면 이종 접합 계면

에서의 전하 전달에 영향을 줄 수 있다. Nb 도핑된 $SrTiO_3$과 WO_3 사이에는 쇼트키 접합이 형성되며 이에 따른 쇼트키 장벽이 두 물질 사이에서의 전자 이동을 제한하는 역할을 한다. 그러나 $LaAlO_3$를 계면 사이에 삽입함으로써 쇼트키 장벽을 없애고 쇼트키 접합을 Ohmic 접합으로 효과적으로 바꿀 수 있다는 사실을 보였다.

셋 째는 태양광 물분해 소자에서 연속된 type II 접합을 이용한 전하 전달 향상 연구이다. 태양광 물분해 소자를 구성하는 광전극 물질은 서로 다른 물질을 이용해 type II 접합 구조를 갖는 이종 접합 구조가 사용되곤 한다. 이 때 연속적인 type II 접합으로 이루어진 이종 접합 구조를 갖도록 세 물질을 적층하면 빛 흡수와 광변환 효율, 전자-홀 전하 분리 능력이 향상된 광전극 물질을 만들 수 있음을 보였다.

본 논문에서는 위 연구들을 통해 산화물 이종 접합 계면에서 전하의 수평 및 수직방향 이동을 제어할 수 있음을 효과적으로 보였다. 이는 전자소자 및 태양광 물분해 소자에 응용될 수

있으며, 차후 이종접합의 성질을 연구함에 있어 기반이 될 수 있는 연구이다.

키워드: 전자, 전하 이동, 광 물분해, 이종 접합, 산화물 박막

학번: 2013-23036

김태민